

# **JGR** Space Physics

## بص

#### RESEARCH ARTICLE

10.1029/2023JA032279

#### **Key Points:**

- Field-aligned currents (FACs) contribute more than particle precipitation to asymmetry in electric potential and Joule heating
- More asymmetry arises from asymmetric distribution rather than asymmetric total magnitude in FACs and precipitation between two hemispheres
- A new asymmetry index can describe the spatial distribution asymmetry, which reveals asymmetric spatial details that are often overlooked

#### **Supporting Information:**

Supporting Information may be found in the online version of this article.

#### Correspondence to:

Y. Deng, yuedeng@uta.edu

#### Citation:

Hong, Y., Deng, Y., Maute, A., Lu, G., Zhu, Q., Waters, C., et al. (2024). Relative contributions of field-aligned currents and particle precipitation to inter-hemispheric asymmetry at high latitudes during the 2015 St. Patrick's Day storm. *Journal of Geophysical Research: Space Physics*, 129, e2023IA032279. https://doi.org/10.1029/2023JA032279

Received 13 NOV 2023 Accepted 31 MAR 2024

© 2024. The Authors.

This is an open access article under the terms of the Creative Commons

Attribution-NonCommercial-NoDerivs

License, which permits use and distribution in any medium, provided the original work is properly cited, the use is non-commercial and no modifications or adaptations are made.

## Relative Contributions of Field-Aligned Currents and Particle Precipitation to Inter-Hemispheric Asymmetry at High Latitudes During the 2015 St. Patrick's Day Storm

Yu Hong<sup>1</sup>, Yue Deng<sup>1</sup>, Astrid Maute<sup>2,3</sup>, Gang Lu<sup>4</sup>, Qingyu Zhu<sup>4,5</sup>, Colin Waters<sup>6</sup>, Cheng Sheng<sup>1</sup>, Ramon Lopez<sup>1</sup>, and Daniel Welling<sup>7</sup>

<sup>1</sup>Department of Physics, University of Texas at Arlington, Arlington, TX, USA, <sup>2</sup>Cooperative Institute for Research in Environmental Sciences, University of Colorado Boulder, Boulder, CO, USA, <sup>3</sup>NOAA Space Weather Prediction Center, Boulder, CO, USA, <sup>4</sup>High Altitude Observatory, National Center for Atmospheric Research, Boulder, CO, USA, <sup>5</sup>William B. Hanson Center for Space Sciences, University of Texas at Dallas, Richardson, TX, USA, <sup>6</sup>Centre for Space Physics, University of Newcastle, Newcastle, NSW, Australia, <sup>7</sup>Climate and Space Sciences and Engineering, University of Michigan, Ann Arbor, MI, USA

**Abstract** High latitude upper atmospheric inter-hemispheric asymmetry (IHA) tends to be enhanced during geomagnetic storms, which may be due to the complex spatiotemporal changes and magnitude modifications in field aligned currents (FACs) and particle precipitation (PP). However, the relative contribution of FACs and PP to IHA in high-latitude forcing and energy is not well understood. The IHA during the 2015 St. Patrick's Day storm has been investigated using the global ionosphere thermosphere model (GITM), driven by FACs from the Active Magnetosphere and Planetary Electrodynamics Response Experiment (AMPERE) and PP from the Assimilative Mapping of Ionospheric Electrodynamics (AMIE). A comprehensive study of the (a) relative contributions of FACs and PP to electric potential and Joule heating and (b) sensitivity of electric potential and Joule heating to the changes in magnitude and distribution of FACs and PP is presented. The results indicate that FACs lead to larger potential and Joule heating changes compared with PP. The spatial variations of potential and Joule heating are also affected by variation in FACs. As for asymmetric magnitude and distribution, it is found that electric potential and Joule heating are more sensitive to changes in the distribution of FACs and PP than the magnitude of FACs and PP. A new spatial asymmetry index (SAI) is introduced, which reveals spatial asymmetric details that are often overlooked by previous studies. This sensitivity study reveals the relative contributions in high-latitude forcing and emphasizes the importance of obtaining accurate FACs and PP in both hemispheres.

**Plain Language Summary** The high-latitude upper atmosphere is highly variable and the coupling processes with the Earth's magnetosphere are very complex. During geomagnetic storms, the high-latitude electrodynamics and energy deposition can differ significantly between the northern and southern hemispheres, while the knowledge of the associated contribution is limited. In this work, leveraging the flexibility of numerical simulation input specifications, we used a physics-based model to investigate the relative contribution of these hemispheric differences in electrodynamics and energy from the field-aligned current (FAC) system and precipitating particle in the auroral area during the 2015 St. Patrick's Day geomagnetic storm. As a full sensitivity study, we also analyzed the respective sensitivities of hemispheric electrodynamics and energy to the changes in hemispheric magnitude and distribution variations. Our study provides insight into how the storm-time enhanced currents and precipitating particles affect the Earth's high-latitude electrodynamics and energy deposition between the two hemispheres.

#### 1. Introduction

Earth's coupled ionosphere-thermosphere (I-T) system can be significantly different between the northern and southern hemispheres, known as the inter-hemispheric asymmetry (IHA). Specifically, IHA can occur when one hemisphere receives more solar irradiation flux (e.g., Chen et al., 2015; Cnossen & Förster, 2016) or more electromagnetic and particle energy from the magnetosphere associated with geomagnetic storms (e.g., Knipp et al., 2021; Pakhotin et al., 2021), resulting from the coupling efficiency with the interplanetary magnetic field (IMF) and solar wind. IHA is also affected by Earth's asymmetric magnetic field configuration (e.g., Laundal et al., 2017) and asymmetries in atmospheric waves from the lower atmosphere (e.g., Rishbeth &

HONG ET AL.

Müller-Wodarg, 2006). Studies have shown that IHA tends to intensify during geomagnetic storms due to global effects of enhanced high-latitude forcing (Zesta et al., 2016). For example, high-latitude electrodynamic forcing is associated with complex temporal and spatial changes, characterized by large-scale anti-sunward convection flows (e.g., Burch et al., 1985; Cousins & Shepherd, 2010; Nishitani et al., 2003; Reiff & Burch, 1985), enhanced ionospheric currents near the auroral region (e.g., Østgaard & Laundal, 2012), and equatorward expansions of the auroral oval (e.g., Cowley & Lockwood, 1992; Fuller-Rowell et al., 1994). Furthermore, asymmetric electrodynamics leads to IHA in Joule heating (e.g., Codrescu et al., 1995; Foster et al., 1983), which contributes to the changes in the thermospheric neutral wind (e.g., Deng & Ridley, 2006; Sivla et al., 2020), neutral mass density (e.g., Aa et al., 2012; Hong et al., 2023; Sutton et al., 2009; Zhu et al., 2023) and large-scale structures in total electron content (TEC) (e.g., Dashora et al., 2019; Zhu, Lu, & Deng, 2022; Zhu, Lu, Mate, et al., 2022).

Field-aligned currents (FACs) and auroral particle precipitation (PP) are two important forcing quantities that contribute to IHA in the high-latitude regions. Early observations (Iijima & Potemra, 1976a) indicated that the FACs system connecting the magnetosphere and ionosphere consists of Region-1 (R-1) and Region-2 (R-2) ring-like current sheets. As a fundamental element that transfers energy and momentum from the magnetosphere to the ionosphere, FACs play an important role in regulating high-latitude ionospheric convection (e.g., Milan et al., 2017; Shi et al., 2020; Tanaka, 2007). Auroral PP can also significantly influence the convection patterns by modifying the ionospheric conductivity (e.g., Southwood & Wolf, 1978). Previous studies have reported hemispheric asymmetry in the auroral current system (e.g., Coxon, Milan, Carter, et al., 2016; Green et al., 2009; Milan et al., 2017). As shown by Østgaard and Laundal (2012), auroral images can be asymmetric between the two hemispheres, which is a significant indicator of hemispheric asymmetry in the auroral currents. However, the role of high-latitude FACs and PP in IHA and their relative contributions to high-latitude forcing and energy deposition remain unclear.

Due to the different coupling efficiency between the magnetosphere-ionosphere-thermosphere (M-I-T) system and solar wind, the storm-time FACs and PP are not distributed symmetrically between the northern and southern hemispheres. For example, seasonal solar irradiation can alter FACs through modifying the ionospheric conductivity (e.g., Green et al., 2009; Newell et al., 1996), while the magnitude of FACs is also influenced by the IMF and solar wind conditions (Ganushkina et al., 2015; Korth et al., 2010). Similarly, auroral precipitating particles appear to exhibit seasonal variations, with more dayside aurora power enhancement during summer compared to winter, which is associated with the large-scale upward FAC (e.g., Liou et al., 2001). During storm main phase, the auroral oval expands equatorward and auroral electrojet intensifies (e.g., Wing et al., 2013). The IMF  $B_v$ significantly impacts the dayside reconnection geometry (e.g., Park et al., 2006; Sonnerup, 1974). Consequently,  $B_{v}$  effects are reflected in the spatial distribution of FACs (e.g., Green et al., 2009; Iijima et al., 1978; Reistad et al., 2020; Weimer, 2001). Recently, Holappa et al. (2020) showed that there is also an explicit  $B_y$ -effect in the flux of electrons precipitating into the ionosphere. Furthermore, it has been found that the distribution of largescale FACs also depends on the IMF orientation (e.g., Anderson et al., 2008; Carter et al., 2016; Green et al., 2009; Korth et al., 2014) and solar zenith angles (e.g., Coxon, Milan, Clausen, et al., 2016 and references therein). Based on these studies, it remains unknown how changes in the magnitude and distribution of FACs and PP between two hemispheres contribute to IHA in high-latitude forcing and energy deposition.

Several studies have examined the correlation between FACs and auroral precipitation (e.g., Arnoldy, 1974; Foster et al., 1989; Knight, 1973; Ohtani et al., 2009; Robinson et al., 2020; Sheng et al., 2019). A statistical study (Xiong et al., 2020) based on Defense Meteorological Satellite Program (DMSP) observations showed that during elevated storm periods, both large-scale FACs and PP fluxes increase and extend equatorward, while for weakly negative  $B_Z$ , noticeable location differences are seen between these two forcing mechanisms. Furthermore, the magnitude and distribution of FACs show clear temporal and spatial variations. They depend not only on the direction of the IMF and magnetospheric sources (Edwards et al., 2017; Iijima & Potemra, 1976a, 1976b) but also on ionospheric conductivity conditions (e.g., Ohtani et al., 2014), which are modulated by auroral precipitation. For instance, studies have shown a close relationship between dayside FAC intensity and ionospheric conductivity (e.g., Haraguchi et al., 2004). Due to the complex connection between FACs and PP, it remains a challenge to quantify their relative contributions to high-latitude forcing and energy solely from observations alone. Therefore, it is helpful to engage numerical experiments to assist in separating the asymmetric responses to FACs and PP. As demonstrated by several previous studies (Hong et al., 2023; Maute et al., 2021; Zhu, Lu, Maute, et al., 2022), the FAC-driven procedure with pre-defined electron precipitation patterns can improve the accuracy of high-latitude forcing and reproduce the storm-time global I-T system response as compared to simulations

HONG ET AL. 2 of 18

driven by empirical models. Utilizing a similar approach, the 2015 St. Patrick's Day storm has been chosen as a test case for simulation since it is a well-studied storm with extensive observations. This allows validation of the simulation results and further elucidates the significance of specifying accurate FACs and PP for both hemispheres.

In particular, this study evaluates the relative contributions of FACs and PP to IHA in the high-latitude electric potential and Joule heating in order to further our understanding of the respective contributions of FACs and PP to the I-T system. Specifically, GITM simulations driven by Active Magnetosphere and Planetary Electrodynamics Response Experiment (AMPERE) FAC data and Assimilative Mapping of Ionospheric Electrodynamics (AMIE) electron precipitation patterns are used to analyze IHA during the 2015 St. Patrick's Day storm, including model-data comparisons of the ion drifts to validate forcing and simulation. Numerical experiments were conducted from two perspectives: (a) the relative contributions of FACs and PP to electric potential and Joule heating and (b) the sensitivity of electric potential and Joule heating to the changes in magnitude and distribution of FACs and PP.

## 2. Methodology

#### 2.1. DMSP Ion Drift

Data from three DMSP satellites, F16, F17 and F18 were used for the model-data comparisons. These spacecraft are in near-polar orbits with an inclination of approximately  $98.8^{\circ}$ , flying in sun-synchronous orbits with a period of  $\sim$ 110 min at an altitude of  $\sim$ 840 km (Rich & Hairston, 1994). The solar local time (SLT) coverage of these three satellites is in the dawn-dusk sector. During the storm on 17 March 2015, F16-18 crossed the equator at approximately 19.7 SLT (ascending track) and 7.7 SLT (descending track). The cross-track ion drift (Vy) data obtained from the onboard Special Sensor for Ions, Electrons, and Scintillation (SSIES) system, with 1s temporal cadence and data flag "1" (indicating most reliable) were used as representative of the ion convection, that is, electric field at high latitudes. The ion drift Vy was first corrected by removing the linear baseline and co-rotation effects, ensuring Vy is zero at  $45^{\circ}$  Imagnetic latitudel (IMLATI). A  $\sim$ 100 km sliding window was then applied to the data to reduce high-frequency fluctuations and extract large-scale ion convection data (Zhu et al., 2020).

#### 2.2. **GITM**

The Global Ionosphere and Thermosphere Model (GITM) is a three-dimensional, first-principles, physics model for the coupled ionosphere-thermosphere system. GITM numerically solves the governing continuity, momentum and energy equations in spherical coordinates (Ridley et al., 2006). GITM self-consistently calculates the density, velocity, and temperature for neutrals, ions and electrons. The model solves the vertical momentum equation for neutral species without assuming hydrostatic equilibrium, which allows the model to better capture the transient phenomena in the auroral zone where large amounts of energy are deposited into the upper atmosphere within a short time-scale (e.g., Deng et al., 2008, 2011; Deng et al., 2021; Lin et al., 2017; Zhu et al., 2017). Additional details about GITM can be found in Ridley et al. (2006).

#### 2.3. High-Latitude and Global Drivers

In this study, the newly developed NCAR 3Dynamo model (hereafter, NCAR-3D, Maute & Richmond, 2017; Maute et al., 2021) was adopted as the ionospheric electrodynamic solver of GITM, to specify the global electric fields based on AMPERE FACs (Waters et al., 2020) and AMIE electron precipitation patterns (Lu, 2017) in the modified magnetic APEX coordinates (Laundal & Richmond, 2017; Richmond, 1995). Briefly, poleward of the high-latitude boundary, the electric fields are specified by FACs along with the prescribed ionospheric conductivity. Equatorward of the boundary, electric fields are mainly driven by the neutral winds (Zhu, Lu, Maute, et al., 2022). Details of the coupling between NCAR-3D and GITM are discussed by Zhu et al. (2019). The AMIE electron precipitation patterns for this storm were based on the Special Sensor of Ultraviolet Spectrographic Imager (SSUSI) data onboard DMSP F16-18, along with ground magnetic perturbations according to the empirical formula of Ahn et al. (1983). Furthermore, AMIE uses the AMPERE magnetic field perturbations (Lu et al., 2020), and our examination indicates that the AMPERE FACs and AMIE precipitation patterns are similar overall.

The FAC-driven procedure and AMPERE FAC data used in this study have been described by Hong et al. (2023). Basically, data points with current density smaller than the noise level (0.2  $\mu$ A/m<sup>2</sup>) are removed. Due to the

HONG ET AL. 3 of 18

21699402, 2024, 4, Downlo

Table 1 Simulation Settings for the Southern Hemisphere (SH) Described in

Simulations	Field-aligned current	Auroral electron precipitation
$R_0 j_S, PP_S$	FAC-driven NCAR-3D (SH)	AMIE Energy Flux (SH)
$R_1 j_S, PP_N$	FAC-driven NCAR-3D (SH)	AMIE Energy Flux (NH)
$R_2 j_N, PP_S$	FAC-driven NCAR-3D (NH)	AMIE Energy Flux (SH)
$R_3 j_N, PP_N$	FAC-driven NCAR-3D (NH)	AMIE Energy Flux (NH)

differences in geomagnetic field magnitude and curvature, a scaling factor of 1.343 is multiplied to map FACs from the measurement height (780 km) to the APEX reference height (110 km). The 10-min window FACs patterns are linearly interpolated into a 1-min cadence and spatially interpolated onto the NCAR-3D grid. The number of regularly spaced grid points along MLAT and magnetic local time (MLT) are 161 and 100, respectively. The MLT grid is uniformly spaced with a 0.24-hr interval, while the MLAT grids are distributed unevenly with larger intervals in the aurora region ( $\sim 2-3^{\circ}$ ) and smaller intervals near the geomagnetic equator ( $\sim 0.5^{\circ}$ ).

In order to capture the spatial variations of AMPERE FAC (1° in MLAT and 1 hr in MLT) and AMIE electron precipitation (1.66° in MLAT and 0.66 hr in MLT), the GITM model was run with a spatial resolution of 1.25° in geographic latitude (GLAT), 5° in geographic longitude (GLON), and 1/3 scale height of the neutral atmosphere in altitude (roughly 1.5 km at 100 km altitude and 15 km at 300 km altitude). The high-latitude forcing update time was 60 s. The time step of GITM simulations was 2 s. IMF, solar wind and F10.7 data from the CDAWeb OMNI website were used for initializing the ionosphere and thermosphere background and pre-run conditions.

#### 2.4. Simulation Set-Up

In order to simulate the relative contribution of FACs (j) and auroral particle precipitation (PP) to the IHAs in high-latitude forcing and energy, four sets of GITM runs  $(R_0 - R_3)$  were carried out, which were driven by different specifications of FACs and PP. A summary of the settings for these runs can be found in Table 1. In this study, the northern hemisphere (NH) was always driven by the unmodified realistic AMPERE FACs and AMIE PP from the NH, while the high-latitude specification of the southern hemisphere (SH) varied. The standard run,  $R_0$  was driven by the unmodified realistic FACs and PP patterns from the SH (denotation: is and PPs), so both FACs and PP were hemispherically asymmetric. For model run R<sub>1</sub>, the SH was specified with FACs from the SH but PP mirrored from the NH to the SH (j<sub>S</sub>, PP<sub>N</sub>), so PP was forced to be symmetric between the NH and SH. Therefore, the difference between  $R_1$  and  $R_0$  indicates the contribution of PP to IHA. For model run  $R_2$ , PP from the SH with FACs mirrored from the NH to SH  $(j_N, PP_S)$  were used to specify the SH, to show the contributions from FACs to the IHA separately. Additionally, R<sub>3</sub> is the controlled run, where both FACs and PP were mirrored from the NH to the SH (j<sub>N</sub>, PP<sub>N</sub>), and is referred to as the combined effects of FACs and PP. As the main form of large-scale electrodynamics and magnetospheric energy, electric fields and Joule heating were chosen to represent the asymmetric consequences of the high-latitude regions. As mentioned in the introduction, FACs and PP typically respond simultaneously to changes in geophysical conditions, and it is very challenging to separate their contributions as they are interconnected. For this study, the variation of FACs and PP was treated separately, which may be an oversimplification. However, this approach can help deduce the first-order estimation of the impacts on high-latitude forcing. By assuming no asymmetry in FACs or PP, their relative contributions can be estimated by mirroring the FACs or PP patterns.

Table 2 lists the settings of the four GITM runs used in the second section. Here, magnitude and distribution refer to modifications to the total integrated value and hemispheric spatial distributions, rather than modifying the values at hemispheric conjugate points. In order to identify the relative sensitivity to asymmetric magnitude (M), the distribution (D) of FACs and PP patterns from the SH ( $D_S$ ) were used, while the magnitude of these was scaled to the same values in the NH (M<sub>N</sub>). This was done by scaling FACs and PP patterns in the SH according to the ratio of the

Table 2 Settings for the Southern Hemisphere (SH) Simulations Described in Section 3.4

Simulations	Field-aligned current	Auroral electron precipitation
$R_0 M_S, D_S$	FAC-driven (SH original)	AMIE (SH original)
$R_4 M_N, D_S$	FAC-driven (scaled w/NH)	AMIE (scaled w/NH)
$R_5 M_S, D_N$	FAC-driven (shaped w/NH)	AMIE (shaped w/NH)
$R_3 M_N D_{,N}$	FAC (mirrored from NH)	AMIE (mirrored from NH)

hemispheric integrated total FAC and hemispheric integrated total participation energy flux, that is, hemispheric power (HP) between the NH and SH, respectively. Likewise, to determine the sensitivity to spatial distributions, the FACs and PP patterns were mirrored from the NH to the SH (D<sub>N</sub>) but remain the same hemispheric integrated magnitude as the SH (M<sub>S</sub>). Therefore, the relative sensitivity to asymmetric forcing M and D can be estimated.

## 3. Results

The analysis comprises four components. Section 3.1 summarizes the geophysical conditions. To validate the simulation, Section 3.2 describes a

HONG ET AL. 4 of 18

21699402, 2024, 4, Downloaded from https://agupubs.onlinelibrary.wiley.com/doi/10.1029/2023JA032279 by Southwest Research Institute, Wiley Online Library on [03/05/2024]. See the Terms and Conditions (https://agupubs.onlinelibrary.wiley.com/doi/10.1029/2023JA032279 by Southwest Research Institute, Wiley Online Library on [03/05/2024]. See the Terms and Conditions (https://agupubs.onlinelibrary.wiley.com/doi/10.1029/2023JA032279 by Southwest Research Institute, Wiley Online Library on [03/05/2024]. See the Terms and Conditions (https://agupubs.onlinelibrary.wiley.com/doi/10.1029/2023JA032279 by Southwest Research Institute, Wiley Online Library on [03/05/2024]. See the Terms and Conditions (https://agupubs.onlinelibrary.wiley.com/doi/10.1029/2023JA032279 by Southwest Research Institute, Wiley Online Library.wiley.com/doi/10.1029/2023JA032279 by Southwest Research Institute, Wiley Online Library.wiley.com/doi/10.1029/2023JA03279 by Southwest Research Institute, Wiley Online Library.wiley.com/doi/10.1029/2023JA03279 by Southwest Research Institute, Wiley

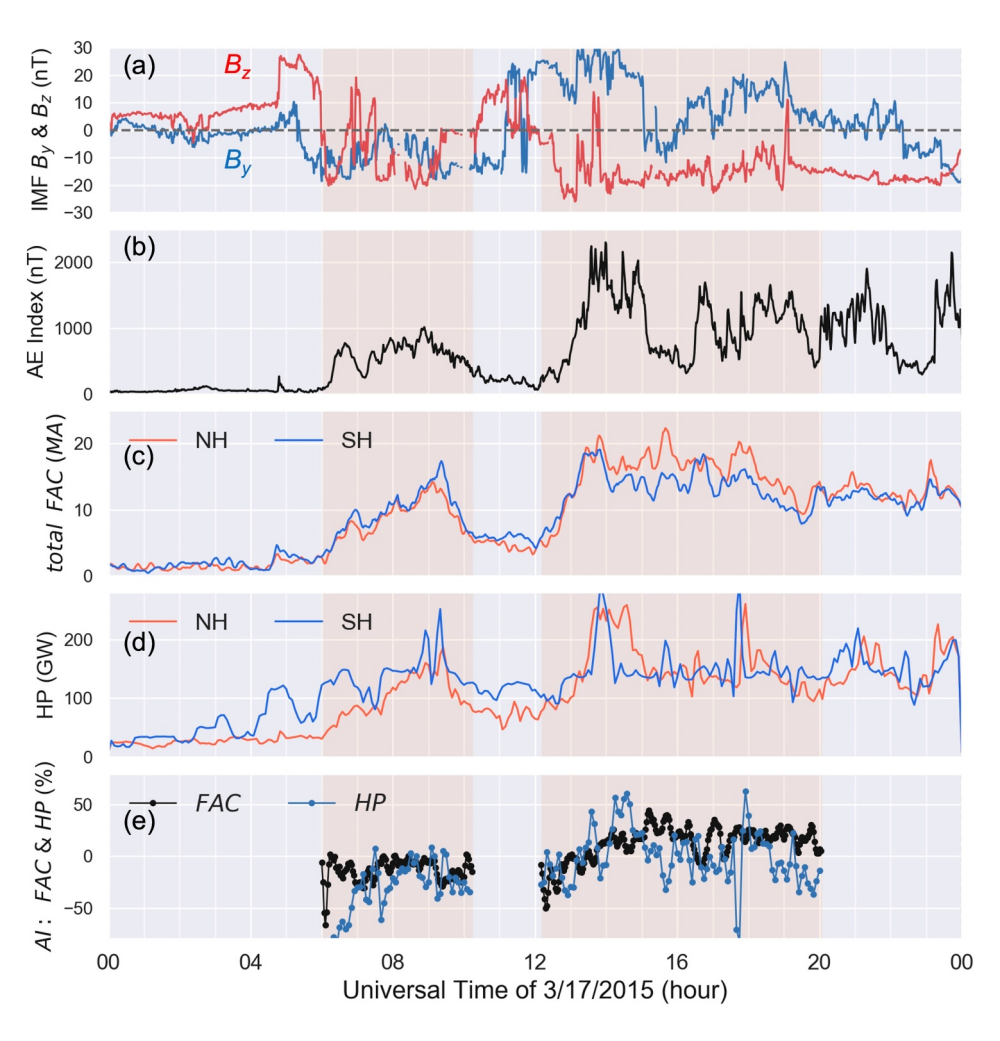


**Figure 1.** (a) Interplanetary magnetic field (IMF) components  $B_y$  and  $B_z$ , (b) aurora electrojet (AE) index, total upward field-aligned current (FAC, (c)) from AMPERE FAC measurements and hemispheric power (HP, (d) from AMIE patterns during the 17 March 2015 St. Patrick's Day storm, for the northern (red lines) and southern (blue lines) hemispheres. The black and blue dotted lines in plot (e) represent the corresponding asymmetry index (AI) for total FAC and HP, respectively. The shaded area highlights the period of interest in this study.

model-data comparison of electric fields at high latitudes. Section 3.3 describes the relative contributions of FACs and PP to high-latitude electric potential and Joule heating. Section 3.4 discusses the sensitivity of potential and Joule heating to the asymmetric magnitude and distribution of FACs and PP.

#### 3.1. Geophysical Conditions

The 2015 St. Patrick's Day storm is a well-known event that has been extensively investigated (e.g., Astafyeva et al., 2015). Figure 1 shows (a) the IMF  $B_y$  (blue) and  $B_Z$  (red) components and (b) auroral electrojet (AE) index on 17 March 2015. As indicated by the two orange shaded areas we focus on in this study, this is a two-step storm (Kamide & Kusano, 2015) with two phases evident in both the evolutions of  $B_Z$  and AE index:

- First storm phase: 06:00 to 10:00 UT, 17 March 2015
- Second storm phase: 12:00 to 20:00 UT, 17 March 2015

In the first phase, IMF  $B_Z$  turned southward at around 06 UT, accompanied by a sudden increase in the AE index. Shortly after,  $B_Z$  reversed to northward for about 40 min, resulting in a slight rebound in the AE index. Starting from 12:20 UT, the storm advanced into the second phase.  $B_Z$  turned southward again and remained southward until the end of the day except for a very short period around 13:30 UT. Accordingly, the AE index reached maxima around 14:00 UT and remained at large values (on average >1,000 nT) until 00UT. During these two

HONG ET AL. 5 of 18

phases,  $B_y$  mostly remained negative in the first phase and positive in the second phase, respectively. This is an interesting feature of this storm, which might lead to asymmetry in high-latitude forcing and magnetospheric energy dissipation.

As a measure of how energy enters and dissipates in the Earth's high-latitude regions due to magnetosphereionosphere (M-I) coupling, Figures 1c and 1d shows the total upward FAC and the total energy flux of precipitating electrons, that is, HP for the northern (red curves) and southern (blue curves) hemispheres. As expected, both total FAC and HP increased to relative maximums during the two southward  $B_Z$  elevated periods, with generally larger values during the second phase. Hong et al. (2021) has developed an asymmetry index (AI) to quantify the IHA for a specific quantity, based on the ratio of hemispheric difference to the two-hemisphere average of global representors, for example, cross-polar-cap potential (CPCP) and total Joule heating. To characterize the features of asymmetric energy deposited into two hemispheres, the same procedure is followed here. Figure 1e gives the AI of total FAC (black dotted) and HP (blue dotted) during the two storm phases. Obvious asymmetries are captured in both quantities. In the first storm phase, FACs and HP show negative AI values, that is, more total FACs and HP in the SH; while during the second storm phase, the FACs exhibit positive AI values, indicating greater total FACs in the NH, except for the initial few hours (12:00 to 13:30 UT). There are more pronounced fluctuations shown in HP, with roughly negative AI, that is, more HP in the SH than that in the NH on average, throughout the storm. In summary, the two inputs FACs and PP, show clear IHAs even at equinox, with significant magnitude differences in total FACs and HP between the northern and southern hemispheres.

#### 3.2. Model-Data Comparison of Ion Convection at High Latitudes

In order to demonstrate the applicability of simulations with AMPERE FAC and AMIE PP for this storm, GITM simulated high-latitude ion drifts were used to compare with the DMSP measured cross-track ion drift Vy, which serves as a proxy for the electric fields. The GITM simulation ion drifts were extracted along the DMSP trajectories at the same location, that is, GLAT, GLON, and then scaled from 400 km to the DMSP altitude (ALT) at ~840 km. The zonal (east-west) and meridional (north-south) ion drifts from GITM were projected onto the along-track and cross-track directions of DMSP trajectories for a direct comparison.

As shown in Figure 2, nine examples from DMSP F16-18 are compared with the corresponding GITM simulations, with the top two and bottom panels representing polar-crossing from the NH and SH. The black dotted lines show the observed Vy, while the red dotted curves represent GITM simulated Vy from the standard run  $R_0$ , that is, driven by realistic FACs and PP patterns in each respective hemisphere. Overall, the consistency between DMSP and GITM indicates that the FAC-driven procedure with AMPERE FACs and AMIE PP can capture the electric fields at high latitudes reasonably well. Although some quantitative differences between data and model do exist, such as the underestimation (Figure 2e) and overestimation (Figure 2g) of the maximum electric fields in GITM, this may be attributed to the uncertainties in FACs and PP. Meanwhile, due to the limited spatial and temporal resolution of the high-latitude drivers, that is, NCAR-3D and AMIE, DMSP can capture higher time cadence and finer structures than GITM simulations. Nevertheless, the cross-track ion drifts Vy at high latitudes from the GITM simulations are consistent with those from the DMSP observations.

### 3.3. Relative Contribution of FACs and PP

To quantify the relative contributions from FACs and PP, a sensitivity index (SI) was defined by comparing the different GITM runs described in Table 1 and Section 2.4. The SI is

$$SI_{j} = \frac{(j_{N}, PP_{S} - j_{S}, PP_{S})}{(j_{N}, PP_{S} + j_{S}, PP_{S})/2} \times 100\%$$
 (1)

$$SI_{PP} = \frac{(j_S, PP_N - j_S, PP_S)}{(j_S, PP_N + j_S, PP_S)/2} \times 100\%$$
 (2)

where, each  $(j_{S/N}, PP_{S/N})$  term denotes the GITM runs with different FACs and PP specifications as described in Section 2.4. The SI index is the ratio between the change of two runs of a variable to the average of these two runs. For a specific variable, the SI index can be identified by substituting that variable from different runs to obtain the

HONG ET AL. 6 of 18



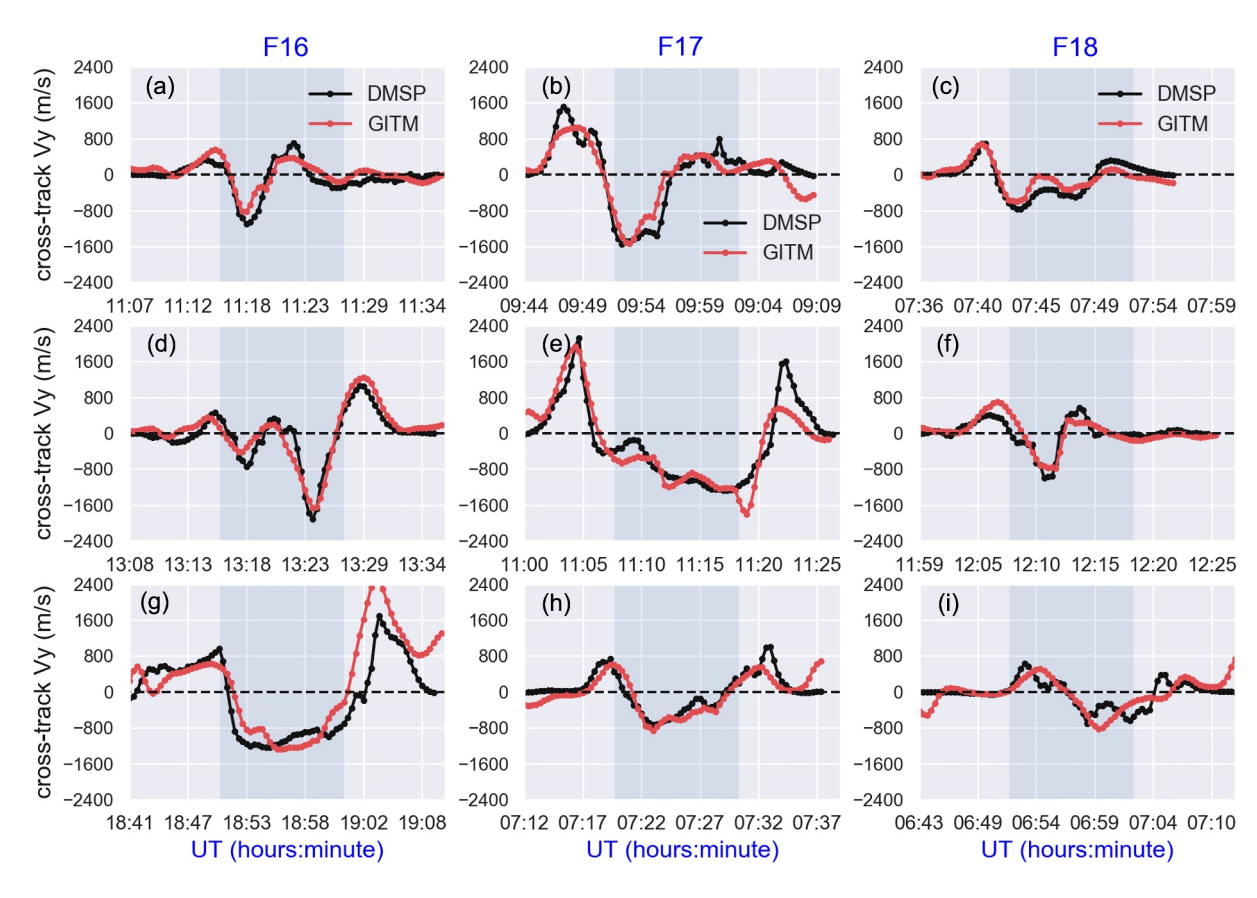


Figure 2. Comparative of nine examples of cross-track ion drifts (Vy) along the Defense Meteorological Satellite Program (DMSP) satellites F16 (left), F17 (middle), and F18 (right) polar trajectories on 17 March 2015. The black dotted lines represent the DMSP results with a 13-point (~100 km) sliding window, the red dotted lines indicate the ion drifts from FAC-driven GITM simulation.

corresponding SI. For simplicity, the focus of this study is changes in the SH. In this study, the values used in Equations 1 and 2 represent global features such as CPCP and hemispheric integrated total Joule heating. Therefore, all terms in Equations 1 and 2 refer to the SH with different FACs and PP specifications (e.g.,  $R_1$ ,  $R_2$ , and  $R_3$ ), and all second terms in the numerator and denominator are the standard run  $R_0$  ( $j_S$ , PP<sub>S</sub>). Specifically, to estimate the relative contribution from FACs, the first term in the numerator and denominator of Equation 1 is the GITM run  $R_2$  ( $j_N$ , PP<sub>S</sub>). Similarly, as for the relative contribution from PP, both the first term in Equation 2 is replaced by GITM  $R_1$  ( $j_S$ , PP<sub>N</sub>). Instead of comparing the NH and SH, the SI here refers to the differences within SH between two GITM runs. Nevertheless, the SI is still related to the IHA since in  $R_1$  and  $R_2$  the PP and FACs used in the SH is mirrored from the NH.

#### (1) Relative contribution of FACs and PP: the spatial perspective

The relative importance of FACs and PP can be evaluated by their respective contributions to electric potential and Joule heating. Figure 3 shows the comparison of FACs (a), (e) and (i), PP (b), (f) and (j), polar cap potential (PCP, (c), (g) and (k)) and height-integrated Joule heating (d, h, l) in the SH at 09 UT on 17 March 2015, for three GITM runs. These are the standard run  $R_0$  (top), mirrored PP  $R_1$  (middle), and mirrored FACs  $R_2$  (bottom). Each panel is displayed in geographic coordinates with GLAT and SLT. Here the SH is viewed as through the Earth from the NH. The maxima and minima values are highlighted in orange and blue, in the lower right and left corners, respectively. As shown in Figure 1, the corresponding AI for total FAC and HP at 09 UT are -5.88% and -30.38%, respectively. This can be seen from the FACs where  $j_s$  has larger maxima (Figures 3a and 3e) compared to  $j_N$  (Figure 3i). As for PP, Figure 3b shows more precipitation near the dusk-side compared with the dawn-side, with a maximum value of 46 erg cm<sup>-2</sup> s<sup>-1</sup> while Figure 3f shows the opposite distribution, with more precipitation near the dawn-side and a maximum value of 21 erg cm<sup>-2</sup> s<sup>-1</sup>. Additionally, 09 UT is during elevated solar wind driving conditions when the IMF was southward ( $B_Z < 0$ ) with strongly negative IMF  $B_y$ . The region-1

HONG ET AL. 7 of 18

21699402, 2024, 4, Downloaded from https://agupubs.onlinelibrary.wiley.com/doi/10.1029/2023JA032279 by Southwest Research Institute, Wiley Online Library on [03/05/2024]. See the Terms and Conditions (https://online

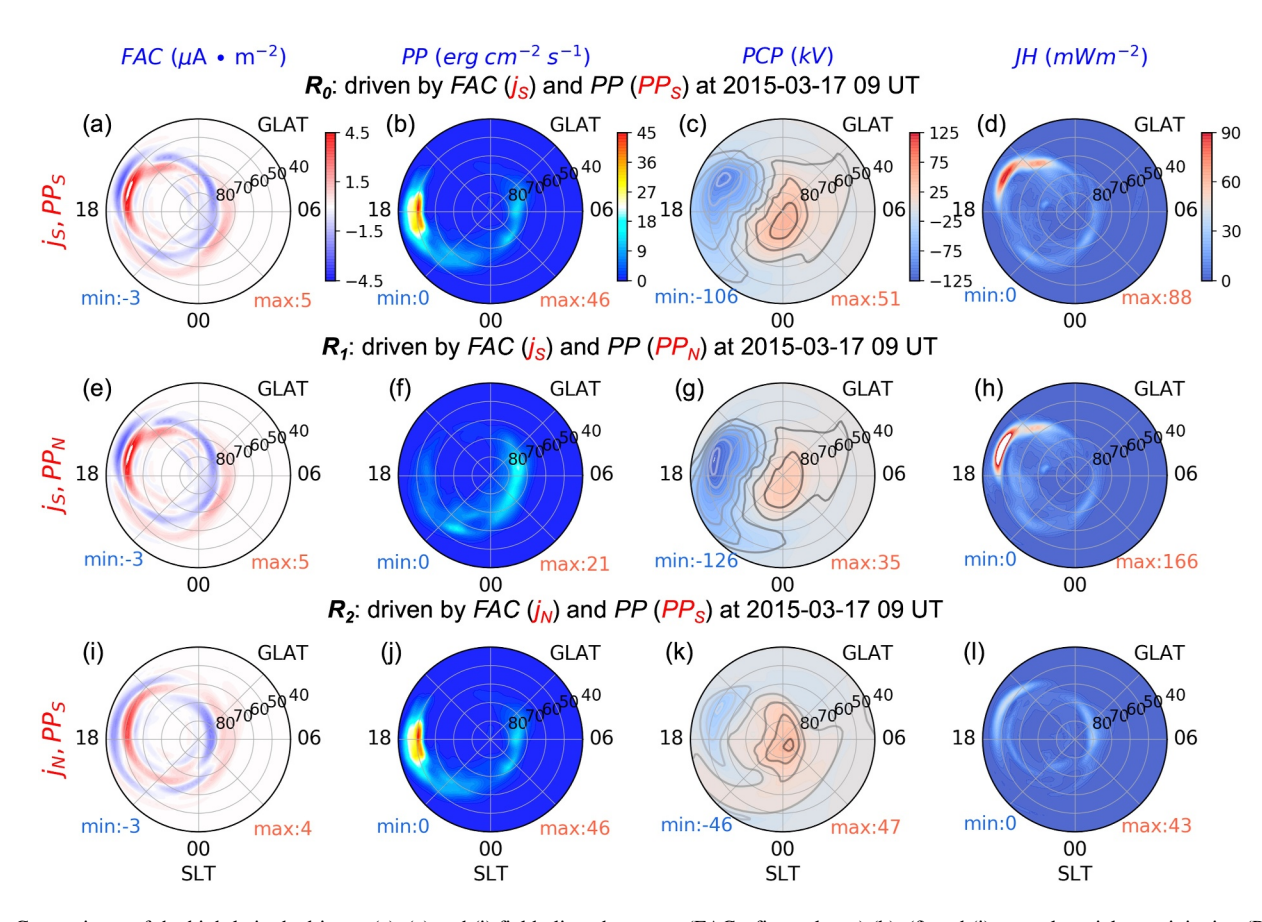


**Figure 3.** Comparisons of the high-latitude drivers. (a), (e) and (i) field-aligned currents (FACs, first column) (b), (f) and (j) auroral particle precipitation (PP, second column), and the corresponding (c), (g) and (k) polar cap potential (PCP, third column) and (d), (h) and (l) height-integrated Joule heating (JH, fourth column) in the southern hemisphere (SH) at 09 UT on 17 March 2015 from different GITM simulations: (a)–(d)  $R_0$  driven by realistic drivers from the SH (j<sub>S</sub>, PP<sub>S</sub>, top row) (e)–(h)  $R_1$  driven by FACs from SH but PP mirrored from the northern hemisphere (NH) (j<sub>S</sub>, PP<sub>N</sub>, middle row), and (i)–(l)  $R_2$  driven by PP from SH but FACs mirrored from the NH (j<sub>N</sub>, PP<sub>S</sub>, bottom row). Each plot displays in the geographic coordinates under geographic latitude (GLAT) and solar local time (SLT). The maxima and minima values are highlighted in orange and blue at the lower right and left corners, respectively. Here the SH is viewed as through the Earth from the NH.

(directed downward at dawn and upward at dusk) and region-2 (directed upward at dawn and downward at dusk) currents can be seen clearly from the AMPERE FACs. The FACs patterns used in  $R_0$  and  $R_2$  (Figure 3i) are from the SH  $j_S$  and mirrored from the NH  $j_N$ , respectively. For negative  $B_y$ , that is,  $B_y$  points dusk-to-dawn, a dusk-side region-1 current streamline surrounds the outside of the dawn-side region-1 current flow in the dayside region (Figure 3i) for  $j_N$ , while for  $j_S$ , a dawn-side region-1 current streamline can be seen in the dayside (Figures 3a and 3e), since the SH responds oppositely to  $B_y$  polarity compared to the NH. The  $B_y$ -responses in FACs are in agreement with previous studies (e.g., Cowley et al., 1991; Iijima et al., 1978). Similarly, the intensified precipitation also depends on the polarity of  $B_y$ , the SH dusk-side PP<sub>S</sub> (Figures 3b and 3j) and NH dawn-side PP<sub>N</sub> (Figure 3f) tend to have larger energy flux. The  $B_y$ -dependent stresses are expected to dominate on newly opened flux tubes, giving rise to the east-west flows just poleward of the open-closed field line boundary, as originally described by Atkinson (1972) and Jørgensen et al. (1972). Overall, the AMPERE FACs and AMIE PP patterns exhibit  $B_y$  dependence at 09 UT.

During geomagnetic storms, the elevated magnetospheric energy input can lead to asymmetric enhancement of FACs and PP between two hemispheres, further promoting IHA in the high-latitude forcing and energy such as electric potential and Joule heating. As shown in Figures 3b and 3f, the PP patterns used for  $R_0$  (PP<sub>S</sub>) and  $R_1$  (PP<sub>N</sub>) are significantly asymmetric between the two hemispheres. However, the two corresponding PCP patterns (Figures 3c and 3g) show similar dawn-dusk asymmetry and the two potential cells are roughly confined to the same spatial locations. In terms of magnitude, a similar potential gradient, that is, CPCP can be found between Figures 3c and 3g for  $R_0$  (157 kV) and  $R_1$  (161 kV) driven by different PP patterns. Similarly, the NH-mirrored PP

HONG ET AL. 8 of 18

pattern leads to no apparent changes in the distribution of Joule heating, but the maxima integrated Joule heating in the 15-18 SLT sector significantly increased from 88 mW m<sup>-2</sup> in  $R_0$  (Figure 3d) to 166 mW m<sup>-2</sup> in  $R_1$ (Figure 3h). The  $R_1$  simulation suggests that this increase can be explained by the same input FACs (Figures 3a and 3e) but smaller PP (Figure 3g vs. Figure 3c) in the same SLT sector. On the other hand, when the FACs change from the SH in  $R_0$  to the NH-mirrored in  $R_2$ , the PCP distributions significantly differ, with an extended positive cell in the dawn to midnight sectors shown in  $R_2$  (Figure 3k). As expected, the two-cell potential pattern emerges with the dominant dusk (dawn) cell for  $B_v < 0$  conditions in the SH (NH). The electric potential shows a sharp decrease in magnitude with CPCP changes from GITM  $R_1$  157 kV (Figure 3c) to GITM  $R_2$  93 kV (Figure 3k). As for the Joule heating shown in Figure 3l, the maximum magnitude decreases from 88 to 43 mW m<sup>-2</sup>, and the distribution significantly differs from  $R_0$ . While there is a dependence between FACs and PP, meaning that PP may also vary with the mapping of FACs, GITM simulations still reveal some fundamental insights. Overall, both FACs and PP can substantially change the magnitude of CPCP and Joule heating, while in terms of spatial distribution, the contributions come primarily from FACs. Ignoring the inconsistency between FACs and PP distributions due to the mirroring process, Figure 3 suggests that FACs are more effective than PP in causing significant changes and IHAs in polar cap electric potential and Joule heating. Moreover, as shown in the supplementary Figure S1 in Supporting Information S1, a quick examination at quiet hour showed that this conclusion still holds.

#### (2) Relative contribution of FACs and PP: the temporal perspective

In order to investigate how FACs and PP change polar cap potential and Joule heating in the temporal perspective during the storm, Figure 4 compares the daily variations of CPCP and total Joule heating for the SH in three GITM runs  $R_0$ - $R_2$ . These are  $(j_S, PP_S)$ ,  $(j_S, PP_N)$ , and  $(j_N, PP_S)$ . Starting with the direct changes of CPCP (Figure 4a), it can be seen that the contribution from PP (difference between black and green dotted lines) is negligible during both storm phases, except for some slight differences around 06:30 UT and 14:30 UT. This is due to the large asymmetries in PP (|AI| > 50%) shown in Figure 1e. Specifically, for the first storm phase when  $PP_S > PP_N$ , the CPCP shown by the green curve  $(j_S, PP_N)$  is a slight increase above the black line  $(j_S, PP_S)$ . This is attributed to the anti-correlation between ionospheric conductance associated with PP and the electric field (or CPCP) for a given FACs according to Ohm's Law. An opposite CPCP response is seen during the second phase when  $PP_S$  is generally smaller than  $PP_N$ , corresponding to the positive AI between 13 and 15 UT shown in Figure 1e. As shown in Figure 4c, the hemispheric integrated total Joule heating exhibits similar changes to CPCP, which is reasonable considering the relation between electric field and Joule heating.

Unlike PP, there are significant differences between the black line  $(j_S, PP_S)$  and the blue line  $(j_N, PP_S)$  in CPCP (Figure 4a) and total Joule heating (Figure 4c) due to mirrored FACs. During the first (second) storm phases, a decrease (increase) can be found, which is associated with  $j_S > j_N (j_S < j_N)$  during the corresponding phase. This is also consistent with the Ohm's Law. To further investigate the sensitivity of IHAs in CPCP and total Joule heating to asymmetric FACs and PP, the temporal variations of sensitivity index are shown in Figure 4b (for CPCP) and Figure 4d (for total Joule heating). Similar to the results mentioned above, during the first storm phase, the sensitivity index of FACs,  $SI_j$  (red lines) is larger than the sensitivity of PP  $SI_{PP}$  (purple lines) even the asymmetry index AI of HP could be greater than the AI of total FAC (as shown in Figure 1e). The maximum  $|SI_j|$  and  $|SI_{PP}|$  are 100% versus 24% for CPCP and 110% versus 25% for total Joule heating, respectively.

During the second phase, similar sensitivity responses can be observed, especially for the total Joule heating, with maximum  $|SI_j|$  of 30% for CPCP and 80% for total Joule heating. When the AI of HP is significantly greater than the total FACs, such as at 14:30 UT (PP: 60% vs. FAC: 12%) and 17:45 UT (PP: -80% vs. FAC: 35%) as indicated by Figure 1e, the SIs of FACs and PP to CPCP and total Joule heating are comparable. In addition, a gray ribbon curve has been added to show the combined contribution of FACs and PP ( $R_3$  in Table 1). Not surprisingly,  $SI_{j\&PP}$  and  $SI_j$  are very close, meaning that when changing FACs and PP together, the primary effect is due to the change of FACs, except for sometimes when the HP has an overwhelming AI value.

Therefore, FACs can more effectively cause IHAs in CPCP and total Joule heating for this particular storm event. This also suggests that the relative contribution to IHA of polar cap electric potential and Joule heating from FACs is considerably larger than that from PP.

HONG ET AL. 9 of 18

21699402, 2024, 4, Downloaded from https://agupubs.onlinelibrary.wiley.com/doi/10.1029/2023JA032279 by Southwest Research Institute, Wiley Online Library on [03/05/2024]. See the Terms and Conditions (https://online

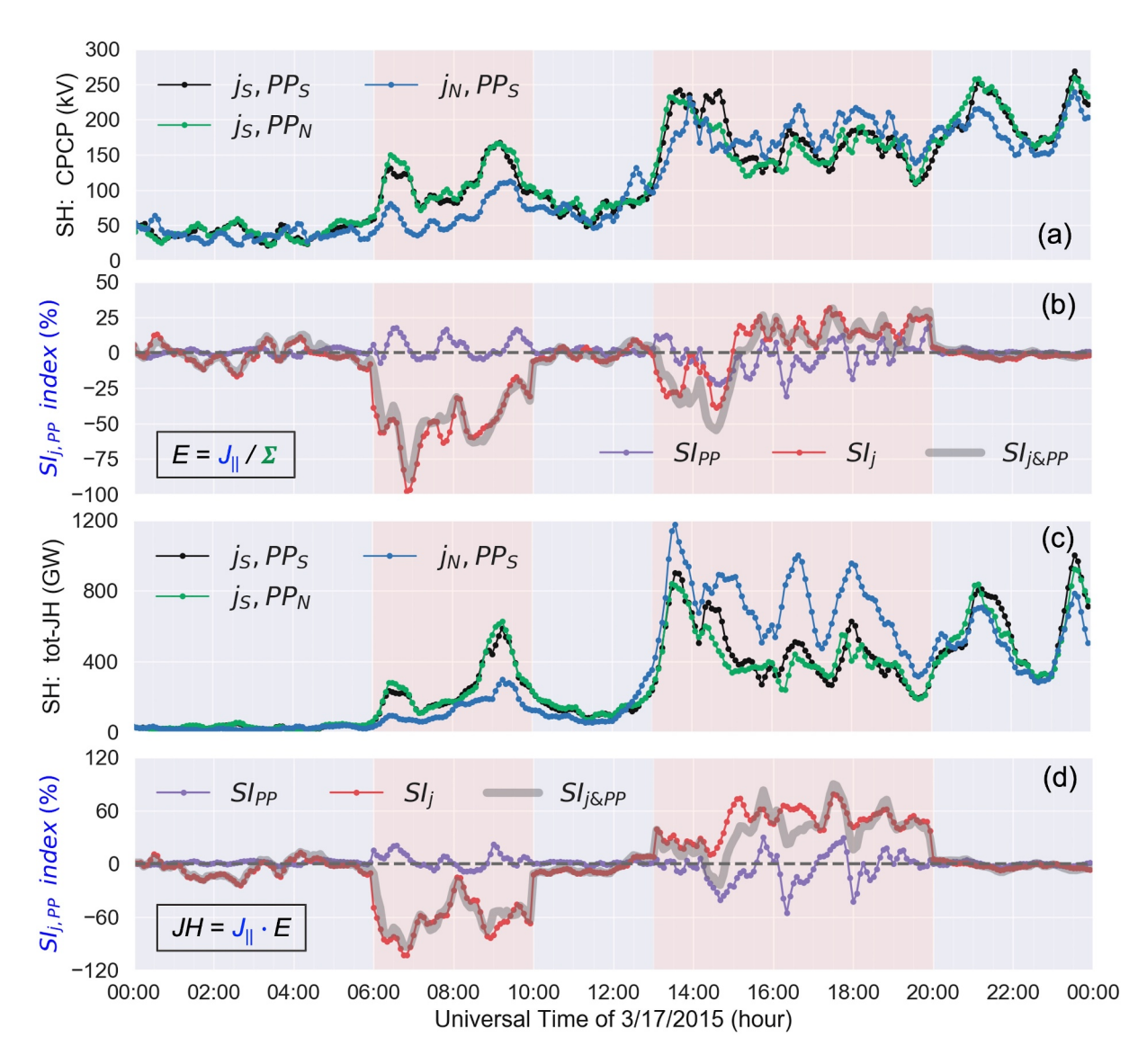


**Figure 4.** Comparisons of southern hemispheric (SH) cross-polar-cap potential (CPCP, (a)) and total Joule heating (tot-JH, (c)) on 17 March 2015 from different GITM runs: driven by realistic drivers from SH ( $j_S$ , PP<sub>S</sub>,  $R_0$ , black dotted lines), driven by field-aligned currents (FACs) from SH but particle precipitation (PP) mirrored from the northern hemisphere (NH) ( $j_S$ , PP<sub>N</sub>,  $R_1$ , green dotted lines), and driven by PP from SH but FACs mirrored from the NH ( $j_N$ , PP<sub>S</sub>,  $R_2$ , blue dotted curves). The corresponding sensitivity index (SI) of PP (SI<sub>PP</sub>), FACs (SI<sub>j</sub>), and combination of FACs and PP (SI<sub>j&PP</sub>) are shown for CPCP (b) and tot-JH (d), respectively. The two shaded regions refer to the southward  $B_Z$  elevated period that is the focus of this study.

#### 3.4. Relative Sensitivity to Magnitude Versus Distribution Changes of FACs and PP

Section 3.3 described the relative contributions of FACs and PP to IHAs in high-latitude forcing and energy. It is worth noting that FACs and PP can be asymmetric in both magnitude and distribution. We now extend the study to investigate the sensitivity of the polar cap electric potential and Joule heating to two fundamental asymmetric characteristics of FACs and PP: magnitude (M) and distribution (D). To quantify the relative sensitivity to magnitude (M) and distribution (D), two new sensitivity indices were defined as

$$SI_M = \frac{(M_N, D_S - M_S, D_S)}{(M_N, D_S + M_S, D_S)/2} \times 100\%$$
 (3)

$$SI_D = \frac{(M_S, D_N - M_S, D_S)}{(M_S, D_N + M_S, D_S)/2} \times 100\%$$
 (4)

HONG ET AL. 10 of 18



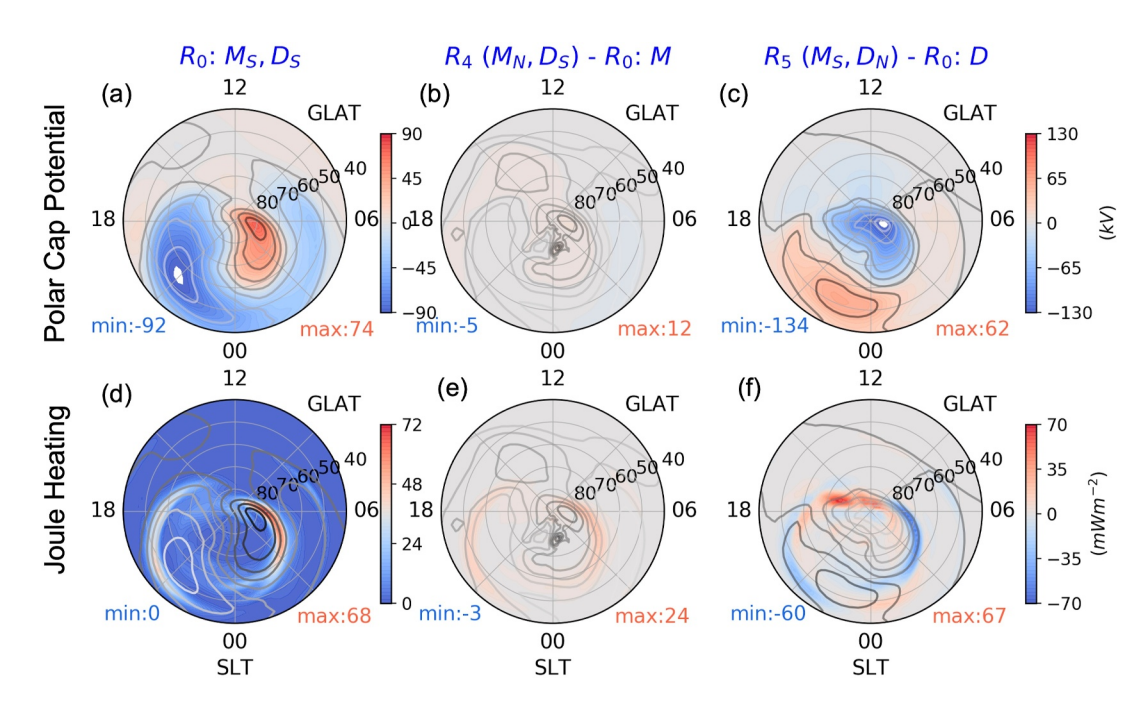


Figure 5. The GITM simulated (a)–(c) polar cap potential and (d)–(f) height-integrated Joule heating in the southern hemisphere (SH) in geographic coordinate at 15 UT on 17 March 2015 from different GITM runs. (a) and (d)  $R_0$  driven by unmodified realistic field-aligned currents (FACs) and particle precipitation (PP) from the SH ( $M_S$ ,  $D_S$ ), (b) and (e) difference between  $R_4$  and  $R_0$ , as in  $R_4$  the FACs and PP magnitude were scaled to the same values in the NH ( $M_N$ ,  $M_S$ ), and (c) and (f) difference between  $M_S$  and  $M_S$  and  $M_S$  are FACs and PP were mirrored from the NH to the SH ( $M_S$ ) but remain the same hemispheric integrated magnitude as the SH ( $M_S$ ).

where each  $(M_{S/N}, D_{S/N})$  term represents a different GITM run, specified in Table 2. The same logic is followed as for Equations 1 and 2, with j and PP replaced by M and D. The second term in both the numerator and denominator is the standard run  $R_0$   $(M_S, D_S)$ . Similarly, to determine the relative sensitivity to M  $(SI_M)$  and D  $(SI_D)$ , the first term can be replaced with GITM runs driven by  $R_4$   $(M_N, D_S)$  and  $R_5$   $(M_S, D_N)$ , respectively.

#### (1) Relative sensitivity of magnitude and distribution: the spatial perspective

As described in Section 2.4 and Table 2, two additional GITM runs were conducted. In order to maintain the consistency between FACs and PP, these runs simultaneously modified the magnitude or distribution of FACs and PP patterns together. Specifically, to investigate the sensitivity to M,  $R_4$  was specified by the FACs and PP patterns from the SH, but the magnitudes were scaled to make the hemispheric integrated total FAC and HP in the SH match those in the NH ( $M_N$ ,  $D_S$ ). Similarly,  $R_5$  was driven by the FACs and PP patterns mirrored from the NH, but the magnitudes of the hemispheric integrated total FAC and HP were scaled to match those in the SH ( $M_S$ ,  $D_N$ ). Thus, the difference between  $R_0$  and  $R_4$  refers to the contribution from asymmetric FACs and PP magnitude (M) on a global basis, while the difference between  $R_0$  and  $R_5$  represents the contribution from global asymmetric FACs and PP distribution (D).

Sensitivity studies were conducted by comparing the two-dimensional (2-D) patterns. Figure 5 shows the PCP and height-integrated Joule heating in the SH at 15 UT on 17 March 2015 for different runs. The left column is from the standard run  $R_0$  ( $M_S$ ,  $D_S$ ), the middle column gives the difference between  $R_4$  ( $M_N$ ,  $D_S$ ) and  $R_0$ , represents the contribution of asymmetric magnitude. The right column presents the difference between  $R_5$  ( $M_S$ ,  $D_N$ ) and  $R_0$ , indicating the contribution of asymmetric distribution. Note that the color-bar scale of  $R_0$  differs from that of the differences ( $R_4 - R_0$ ) and ( $R_5 - R_0$ ), in order to provide the best visual display. For comparative analyses, the potential contour lines were mapped to the corresponding Joule heating patterns in the bottom row, where the color represents Joule heating, and contour lines represent the PCP. Figures 5b and 5e illustrate the sensitivity to asymmetric magnitude: both PCP and Joule heating patterns in  $R_4$  closely follow the distributions shown in  $R_0$ . The changes due to asymmetric magnitude ( $R_4 - R_0$ ) is 10 kV in CPCP (176–166 kV), and the maximum difference in height-integrated Joule heating is 24 mW m<sup>-2</sup>. In contrast, both spatial distribution and magnitude of

HONG ET AL. 11 of 18

21699402, 2024, 4, Downloaded from https://agupubs.onlinelibrary.wiley.com/doi/10.1029/2023JA032279 by Southw

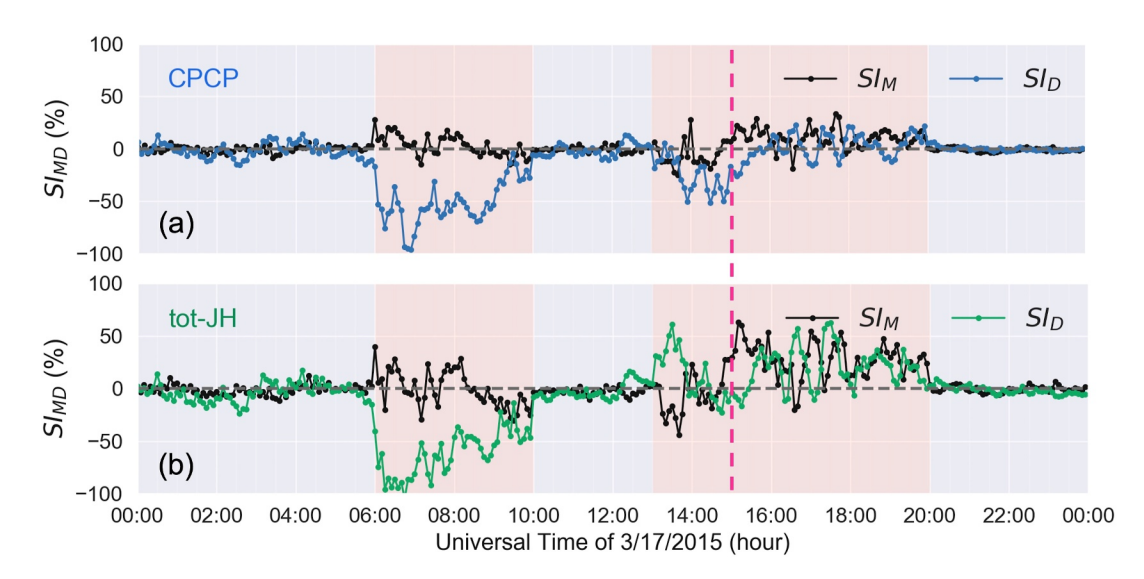


Figure 6. Time series of the magnitude sensitivity index ( $SI_{M}$ ) and distribution sensitivity index ( $SI_{D}$ ) due to the modified high-latitude drivers. The (a) top (b, bottom) plot is for the cross-polar-cap potential CPCP (total Joule heating). The shaded regions refer to the southward  $B_{Z}$  elevated period that is the focus of this study. The vertical pink dashed line represents the time used for plotting the contours at 15 UT in Figure 5.

PCP and Joule heating are sensitive to changes in FACs and PP distribution. The difference due to asymmetric distribution ( $R_5$  -  $R_0$ ) shown in Figures 5c and 5f primarily manifest as a day-night structure rather than the dawndusk cells depicted in Figure 5a. The change of the CPCP value is -27 kV (139–166 kV), while the maximum variation for Joule heating can be 67 mW m<sup>-2</sup>. It is apparent that altering the asymmetric distribution of FACs and PP can effectively modify high-latitude forcing and energy in distribution and magnitude at specific locations. In contrast, the asymmetric magnitude of FACs and PP seems to cause only small changes. Furthermore, when scaling the magnitude, FACs and PP patterns were scaled separately according to the respective ratio of the hemispheric integrated FACs and HP between the two hemispheres. The quantitative results for this specific case may not be universal, but the qualitative results, such as the asymmetry in distribution plays a more important role than the asymmetry in magnitude, can be universal.

#### (2) Relative sensitivity of magnitude and distribution: the temporal perspective

Since Figure 5 only shows snapshots of the PCP and Joule heating at a specific time, Figure 6 displays the temporal variations of sensitivity index SI for CPCP and total Joule heating with respect to asymmetric magnitude (black dotted lines) and distribution (blue and green dotted curves) of FACs and PP. Similarly, the upper (lower) panel corresponds to CPCP (total Joule heating). The ordinate is the  $SI_{MD}$  for magnitude (M) and distribution (D). Specifically, a positive (negative)  $SI_{M}$  implies that there is an increase (decrease) of CPCP or total Joule heating at specific times due to the asymmetric FACs and PP magnitude. On the other hand, it can be more challenging to relate the  $SI_{D}$  index to physical processes. In simple terms,  $SI_{D}$  can be regarded as the variation of CPCP and total Joule heating due to the asymmetric distribution.

The relative sensitivity to asymmetric magnitude and distribution can be identified from each panel in Figure 6. During the first storm phase, the sensitivity of the CPCP and total Joule heating to asymmetric distribution  $SI_D$  is considerably larger than the sensitivity to asymmetric magnitude  $SI_M$ . During the second storm phase, the  $SI_D$  is still roughly larger than  $SI_M$  for the CPCP but could be comparable or smaller than  $SI_M$  for total Joule heating (e.g., 15 UT). This suggests that more pronounced asymmetries in distribution of FACs and PP could be captured during the first phase. More details are discussed in Section 4. Overall, for this storm, the changes due to modified FACs and PP distribution are greater than the changes due to modified magnitude, especially for the first storm phase. A relevant aspect here is that the geomagnetic field configuration does play a role in the "D" effect, such as the distribution asymmetry caused by the asymmetric magnetic field strength at conjugate points, and the different pole locations between the NH and SH. However, the asymmetry of geomagnetic field configuration between the two hemispheres may partially contribute to the impact of D, since this study is focused on large-scale effects

HONG ET AL. 12 of 18

these smaller scale contributions to D will not play a dominant role. Furthermore,  $SI_M$  of CPCP and total Joule heating exhibit similar positive and negative trends, with the  $SI_M$  changes of Joule heating showing a more prominent variation compared to CPCP. As for  $SI_D$ , the changes for CPCP and total Joule heating may exhibit opposite behavior, as seen during 13–15 UT, where  $SI_D$  is in general negative for CPCP but positive for total Joule heating. Our study also found that the variations of  $SI_M$  and  $SI_D$  can be opposite to each other.

#### 4. Discussion

In order to quantitatively determine the IHA of the I-T system, the simplest approach is to calculate the AI based on global representors. In previous sections, the AI of CPCP and total Joule heating were used to represent the asymmetry of the polar cap potential and Joule heating. However, this approach is insufficient to reveal the spatial distribution details. For example, two very different potential patterns can have the same CPCP. To improve upon this, a spatial asymmetry index (SAI) based on the 2-D correlation of the distributions was introduced. The SAI is defined as

$$SAI = \left\{ 1 - \frac{\Sigma_{x}\Sigma_{y} \left[ \left( N_{xy} - \overline{N} \right) \left( S_{xy} - \overline{S} \right) \right]}{\sqrt{\left[ \Sigma_{x}\Sigma_{y} \left( N_{xy} - \overline{N} \right)^{2} \right] \left[ \Sigma_{x}\Sigma_{y} \left( S_{xy} - \overline{S} \right)^{2} \right]}} \right\} \times 100\%$$
 (5)

where,  $N_{xy}$  and  $S_{xy}$  are the given quantities represented as 2-D arrays for the NH and SH, such as FACs and PCP organized in the latitude-longitude coordinate.  $\overline{N}$  and  $\overline{S}$  are the averages of the given quantities in each hemisphere, and the sigma symbol is the sum of the quantity. Equation 5 is the 2-D correlation coefficient, with the covariance of the two quantities  $N_{xy}$  and  $S_{xy}$  in the numerator and the standard deviation of these two quantities in the denominator. Taking into account the displacement between geographic and geomagnetic coordinates, all quantities were calculated in geomagnetic coordinates. Here, x and y have resolutions of 1.25° in MLAT and 1/3 hr in magnetic local time (MLT). Because the greater the correlation the smaller the asymmetry, an 1 minus was added on the right-hand side of Equation 5. For example, when the distributions in both hemispheres are perfectly correlated, SAI equals 0, which corresponds to  $R_5$ . The SAI primarily depends on spatial distributions. The spatial resolution may have some influence on SAI, since the current resolution is sufficient to capture the large-scale variations and therefore the impact of spatial resolution can be neglected. Furthermore, various methods have been used to quantify the distribution of IHA, such as measuring auroral oval shape (e.g., Milan et al., 2009) and FACs boundary (e.g., Burrell et al., 2020). Nevertheless, the SAI defined in this study may provide a reference point for more comprehensive methods.

To establish the connection via SAI, Figure 7 compares the SAI of PCP (blue curves) and Joule heating (green curves) patterns with the SAI of FACs (top, black dotted curves) patterns and PP (bottom, black dotted curves) patterns in the same format. Spatial patterns of a given quantity may be significantly different between the two hemispheres under quiet conditions, because the distribution can be more irregular than that during storm time. However, mechanisms other than FACs and particle precipitation can play more significant roles in quiet time, resulting in a large SAI index value during quiet times. Thus the focus for this study is the two storm phases indicated by the shaded area. First, the SAI of PCP exhibits considerable changes from 15% to 120% during the first phase, while remaining relatively stable between 40% and 75% during the second phase, indicating that PCP undergoes greater distribution IHAs during the first storm phase. The SAI variation is consistent with the larger SI<sub>D</sub> (Figures 5g and 5h) during the first phase compared with the second phase. Regarding FACs and PP, FACs have, in general, larger spatial asymmetry between the two hemispheres. During the first phase, the SAI of FACs and PP are around 40%-120% and 10%-50%, respectively. While during the second phase, it is around 40%-96% for FACs and 10%-60% for PP. The results from the previous section showed the significant effect of FACs on the distribution of PCP. One would expect a coincidence between these two quantities. The SAI of FACs and PCP have fairly similar variations during the first phase, and similarities persist during the second phase. Overall, the distribution asymmetry of PCP is more dominated by FACs rather than PP, typically during the first storm phase.

For Joule heating (purple dotted curves), the SAI during the first and second phases ranged from 35% to 60% and 20%–70%, respectively, with slightly greater distributional asymmetry during the second phase. The SAIs of Joule heating and FACs exhibit similar variations during 08–10 and 13–15 UTs, while for other times, the SAI of

HONG ET AL.

21699402, 2024, 4, Downlo

Research Institute, Wiley Online Library on [03/05/2024]. See the Term

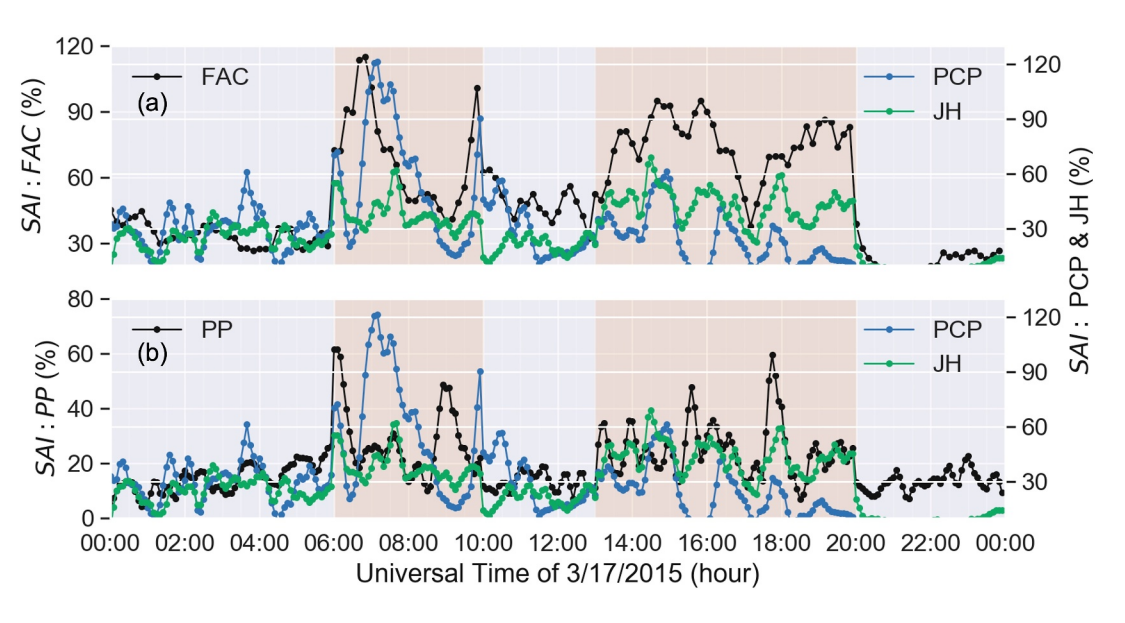


Figure 7. Time series comparisons of spatial asymmetry index (SAI) between the high-latitude drivers, field-aligned currents (FACs, blue lines) and auroral particle precipitation (PP, green lines), as well as the high-latitude forcing polar cap potential (PCP) and energy Joule heating (JH) on 17 March 2015. The top (bottom) panel is for comparing with FACs (PP). The shaded regions refer to the southward  $B_z$  elevated period that is the focus of this study.

PP and Joule heating perform more similarities than or comparable as compared with FACs. This comparison suggests that in this storm, the FACs and PP distribution contribute similarly to the distribution of Joule heating.

Furthermore, the peak SAI of PCP ( $\sim$ 120%) occurs around 07:20 UT, when the NH and SH are mostly asymmetric. However, at the same time, the distribution sensitivity index,  $\mathrm{SI}_{\mathrm{D}}$  does not exceed 50% (see Figure 5a blue line). Similarly, the SAI of Joule heating aligns with peaks around 07:20, 14:30, and 18 UT, while no apparent changes could be captured in  $\mathrm{SI}_{\mathrm{D}}$  from Figure 5b (green line), which is based on the total Joule heating. This result indicates that the maximum asymmetry of CPCP or total Joule heating does not necessarily correspond to the time when the distributional asymmetry is maximized on a spatial basis. Therefore, it might be insufficient to use CPCP or total Joule heating alone as a representative for the asymmetry of PCP and Joule heating.

In addition, the overall behavior of SAI may differ from the general AI, as the latter is based on relative magnitudes and may not include spatial distribution details. For example, the peak SAI of PP can be found at 09, 16 and 18 UT, while the AI at those times may not be significant. On the other hand, both SAI and AI can be large, such as around 17:45 UT for PP and 15:45 UT. When comparing the variations of the two sets of high-latitude forcing with the IMF conditions, it is evident that the IMF  $B_Z$  and  $B_y$  play important roles in the SAI of the high-latitude forcing. For instance, during the period of 07:00-07:30 UT, when a northward  $B_Z$  is captured, the spatial distribution SAI of FACs and PP between the two hemispheres are mostly asymmetric.

### 5. Summary

This study investigated the relative contributions of FACs and PP and the modified magnitude and distribution to IHAs in high-latitude electric potential and Joule heating by driving GITM simulation with different FACs and PP specifications during the 2015 St. Patrick's Day storm. This study used different FACs and PP settings to drive GITM. In the standard run, the SH was driven by realistic FACs and PP from the SH. In the modified runs, the mirrored FACs or PP patterns from the NH were used to drive the SH so that the relative contributions can be separated. The findings regarding the relative contributions of FACs and PP for this specific storm event are summarized as follows:

 Modified FACs contribute more than PP to the IHAs in electric potential and Joule heating, though FACs and PP both have effects on the magnitude of potential and Joule heating at specific locations.

HONG ET AL. 14 of 18

15 of 18



Acknowledgments

This study makes use of NASA OMNI data. This work at UTA was supported by

NASA through Grants 80NSSC20K1786,

80NSSC23K1062, and 80GSFC22CA011, and AFOSR through awards FA9559-16-

1-0364, FA9550-23-1-0634, and FA9550-

National Center for Atmospheric Research (NCAR) Advanced Study Program (ASP)

Graduate Visitor Program Fellowship. AM

23-1-0614. YH was supported by the

80NSSC20K1784 and AFOSR award FA9550-17-1-0248. GL was supported by NASA Grants 80NSSC17K071 and 80NSSC21K1673. QZ was supported by

the NCAR ASP Postdoctoral Fellowship. QZ and GL were also supported by the

NASA Grant 80NSSC22K0061 through

the subaward 2021GC1619. We thank the

AMPERE team and the AMPERE Science

derived from the Iridium Communications

constellation, enabled by support from the

material is based upon work supported by

1852977. This research was supported by

the International Space Science Institute

(ISSI), through ISSI International Team

Ionosphere-Thermosphere Interaction).

The authors would like to acknowledge

the Texas Advanced Computing Center

(TACC, http://www.tacc.utexas.edu) at the

University of Texas at Austin for providing

HPC resources that have contributed to the

research results reported within this paper.

HONG ET AL.

high-performance computing support from NCAR Cheyenne (https://doi.org/10.5065/D6RX99HX). The authors acknowledge

project #511 (Multi-Scale Magnetosphere-

National Science Foundation. This

the National Center for Atmospheric Research, which is a major facility

sponsored by the National Science Foundation under Cooperative Agreement

Data Center for providing data products

was supported by NASA Grant

## **Journal of Geophysical Research: Space Physics**

10.1029/2023JA032279

Modified FACs can more effectively modify the spatial distribution of electric potential and Joule heating than
PP. Despite the smaller asymmetry in total FACs compared to HP, the relative contribution of FACs remains
considerably higher than PP.

Both magnitude and distribution of FACs and PP can be significantly asymmetric during storms. The sensitivity of electric potential and Joule heating to asymmetric magnitude and distribution of FACs and PP was further investigated in this study. To keep the spatial correlation between FACs and PP, they are modified simultaneously. The results reveal that for this specific storm event:

- Asymmetric distribution is more effective in altering the magnitude, distribution, and intensity of electric potential and Joule heating than asymmetric magnitude.
- A new index SAI is used to quantify the asymmetric distribution. The comparison between FACs and PP, and PCP and Joule heating showed a connection of their asymmetric distribution.
- The maximum AI for CPCP and total Joule heating does not coincide with the asymmetry maximized on spatial basis (SAI) for electric potential and Joule heating.

In summary, the standard AI calculations based on CPCP and total Joule heating are insufficient to describe the asymmetry between hemispheres. When quantifying IHA, the standard AI can serve as an indicator, as demonstrated in previous studies. However, when dealing with detailed spatial distribution asymmetries, it is necessary to use SAI as a supplement. Furthermore, given the focus of this paper on the 2015 St. Patrick's Day storm, it would be desirable to explore the relative contributions to IHAs under other seasonal conditions and storm cases in the future.

#### **Data Availability Statement**

The GITM model is open source and can be found at (Ridley, 2021). The Python package spacepy was used to analyze outputs from GITM simulations, which can be found at (Larsen et al., 2021). All data used in this publication are publicly accessible. The IMF, solar wind and AE index used in this study are from NASA OMNI dataset at <a href="https://omniweb.gsfc.nasa.gov">https://omniweb.gsfc.nasa.gov</a>. The DMSP ion drift data can be obtained from <a href="http://cedar.open-madrigal.org/list">https://cedar.open-madrigal.org/list</a>. AMPERE FAC data can be viewed and downloaded at <a href="http://ampere.jhuapl.edu/">https://cedar.open-madrigal.org/list</a>. AMPERE FAC data can be viewed and downloaded at <a href="http://ampere.jhuapl.edu/">https://ampere.jhuapl.edu/</a>. The NCAR 3Dynamo model is not stand-alone, but has been coupled into GITM already. The data files used to generate the plots shown in this publication, including the GITM simulation outputs, and the AMIE patterns used to drive the GITM simulations are available at (Hong, 2023) <a href="https://zenodo.org/records/10067390">https://zenodo.org/records/10067390</a>.

#### References

Aa, E., Ridley, A. J., Zhang, D., & Xiao, Z. (2012). Analyzing the hemispheric asymmetry in the thermospheric density response to geomagnetic storms. *Journal of Geophysical Research*, 117(A8), A08317. https://doi.org/10.1029/2011JA017259

Ahn, B.-H., Robinson, R. M., Kamide, Y., & Akasofu, S.-I. (1983). Electric conductivities, electric fields and auroral energy injection rate in the auroral ionosphere and their empirical relations to the horizontal magnetic disturbances. *Planetary and Space Science*, 31(6), 641–653. https://doi.org/10.1016/0032-0633(83)90005-3

Anderson, B. J., Korth, H., Waters, C. L., Green, D. L., & Stauning, P. (2008). Statistical Birkeland current distributions from magnetic field observations by the Iridium constellation. *Annales de Geophysique*, 26(3), 671–687. https://doi.org/10.5194/angeo-26-671-2008

Arnoldy, R. L. (1974). Auroral particle precipitation and Birkeland currents. *Reviews of Geophysics*, 12(2), 217–231. https://doi.org/10.1029/RG012i002p00217

Astafyeva, E., Zakharenkova, I., & Förster, M. (2015). Ionospheric response to the 2015 St. Patrick's Day storm: A global multi-instrumental overview. *Journal of Geophysical Research: Space Physics*, 120(10), 9023–9037. https://doi.org/10.1002/2015JA021629

Atkinson, G. (1972). In K. Folkestadt (Ed.), Magnetospheric flows and substorms, Magnetosphere-ionosphere interactions (Vol. 203, pp. 203–216). Universitetsforlaget.

Burch, J. L., Reiff, P. H., Menietti, J. D., Heelis, R. A., Hanson, W. B., Shawhan, S. D., et al. (1985). IMF By -dependent plasma flow and Birkeland currents in the dayside magnetosphere: 1. Dynamics explorer observations. *Journal of Geophysical Research*, 90(A2), 1577–1593. https://doi.org/10.1029/JA090iA02p01577

Burrell, A. G., Chisham, G., Milan, S. E., Kilcommons, L., Chen, Y.-J., Thomas, E. G., & Anderson, B. (2020). AMPERE polar cap boundaries. Annales de Geophysique, 38(2), 481–490. https://doi.org/10.5194/angeo-38-481-2020

Carter, J. A., Milan, S. E., Coxon, J. C., Walach, M.-T., & Anderson, B. J. (2016). Average field-aligned current configuration parameterized by solar wind conditions. *Journal of Geophysical Research: Space Physics*, 121(2), 1294–1307. https://doi.org/10.1002/2015JA021567

Chen, Y., Liu, L., Le, H., Wan, W., & Zhang, H. (2015). Dusk-to-nighttime enhancement of mid-latitude NmF2 in local summer: Interhemispheric asymmetry and solar activity dependence. *Annales de Geophysique*, 33(6), 711–718. https://doi.org/10.5194/angeo-33-711-2015
 Cnossen, I., & Förster, M. (2016). North-south asymmetries in the polar thermosphere-ionosphere system: Solar cycle and seasonal influences. *Journal of Geophysical Research: Space Physics*, 121(1), 612–627. https://doi.org/10.1002/2015JA021750

Codrescu, M. V., Fuller-Rowell, T. J., & Foster, J. C. (1995). On the importance of E-field variability for Joule heating in the high-latitude thermosphere. Geophysical Research Letters, 22(17), 2393–2396. https://doi.org/10.1029/95GL01909



## Journal of Geophysical Research: Space Physics

- 10.1029/2023JA032279
- Cousins, E. D. P., & Shepherd, S. G. (2010). A dynamical model of high-latitude convection derived from SuperDARN plasma drift measurements. *Journal of Geophysical Research*, 115(A12), A12329. https://doi.org/10.1029/2010JA016017
- Cowley, S. W. H., & Lockwood, M. (1992). Excitation and decay of solar wind-driven flows in the magnetosphere-ionosphere system. Annales de Geophysique, 10(1–2), 103–115.
- Cowley, S. W. H., Morelli, J. P., & Lockwood, M. (1991). Dependence of convective flows and particle precipitation in the high-latitude dayside ionosphere on the X and Y components of the interplanetary magnetic field. *Journal of Geophysical Research*, 96(A4), 5557–5564. https://doi. org/10.1029/90JA02063
- Coxon, J. C., Milan, S. E., Carter, J. A., Clausen, L. B. N., Anderson, B. J., & Korth, H. (2016). Seasonal and diurnal variations in AMPERE observations of the Birkeland currents compared to modeled results. *Journal of Geophysical Research: Space Physics*, 121(5), 4027–4040. https://doi.org/10.1002/2015JA022050
- Coxon, J. C., Milan, S. E., Clausen, L. B. N., Anderson, B. J., & Korth, H. (2016). The magnitudes of the regions 1 and 2 Birkeland currents observed by AMPERE and their role in solar wind-magnetosphere-ionosphere coupling. *Journal of Geophysical Research: Space Physics*, 119(12), 9804–9815. https://doi.org/10.1002/2014JA020138
- Dashora, N., Suresh, S., & Niranjan, K. (2019). Interhemispheric asymmetry in response of low-latitude ionosphere to perturbation electric fields in the main phase of geomagnetic storms. *Journal of Geophysical Research: Space Physics*, 124(8), 7256–7282. https://doi.org/10.1029/ 2019JA026671
- Deng, Y., Fuller-Rowell, T. J., Akmaev, R. A., & Ridley, A. J. (2011). Impact of the altitudinal Joule heating distribution on the thermosphere. Journal of Geophysical Research, 116(A5), A05313. https://doi.org/10.1029/2010JA016019
- Deng, Y., Lin, C., Zhu, Q., & Sheng, C. (2021). Influence of non-hydrostatic processes on the ionosphere-thermosphere. In W. Wang & Y. Zhang (Eds.), Space physics and aeronomy collection Volume 4: Upper atmosphere dynamics and energetics, Chap. 4, Geophysical Monograph Series (Vol. 261). AGU. https://doi.org/10.1002/9781119815631.ch4
- Deng, Y., Richmond, A. D., Ridley, A. J., & Liu, H.-L. (2008). Assessment of the non-hydrostatic effect on the upper atmosphere using a general circulation model (GCM). *Geophysical Research Letters*, 35(1), L01104. https://doi.org/10.1029/2007GL032182
- Deng, Y., & Ridley, A. J. (2006). Dependence of neutral winds on convection E-field, solar EUV, and auroral particle precipitation at high latitudes. *Journal of Geophysical Research*, 111(A9), A09306. https://doi.org/10.1029/2005JA011368
- Edwards, T. R., Weimer, D. R., Tobiska, W. K., & Olsen, N. (2017). Field-aligned current response to solar indices. *Journal of Geophysical Research: Space Physics*, 122(5), 5798–5815. https://doi.org/10.1002/2016JA023563
- Foster, J. C., Fuller-Rowell, T., & Evans, D. S. (1989). Quantitative patterns of large-scale field-aligned currents in the auroral ionosphere. *Journal of Geophysical Research*, 94(A3), 2555–2564. https://doi.org/10.1029/JA094iA03p02555
- Foster, J. C., St-Maurice, J.-P., & Abreu, V. J. (1983). Joule heating at high latitudes. *Journal of Geophysical Research*, 88(A6), 4885–4897. https://doi.org/10.1029/JA088iA06n04885
- Fuller-Rowell, T. J., Codrescu, M. V., Moffett, R. J., & Quegan, S. (1994). Response of the thermosphere and ionosphere to geomagnetic storms. Journal of Geophysical Research, 99(A3), 3893–3914. https://doi.org/10.1029/93JA02015
- Ganushkina, N. Y., Liemohn, M. W., Dubyagin, S., Daglis, I. A., Dandouras, I., De Zeeuw, D. L., et al. (2015). Defining and resolving current systems in geospacer. *Annales de Geophysique*, 33(11), 1369–1402. https://doi.org/10.5194/angeo-33-1369-2015
- Green, D. L., Waters, C. L., Anderson, B. J., & Korth, H. (2009). Seasonal and interplanetary magnetic field dependence of the field-aligned currents for both Northern and Southern Hemispheres. *Annales Geophysicae*, 27(4), 1701–1715. https://doi.org/10.5194/angeo-27-1701-2009
- Haraguchi, K., Kawano, H., Yumoto, K., Ohtani, S., Higuchi, T., & Ueno, G. (2004). Ionospheric conductivity dependence of dayside region-0, 1, and 2 field-aligned current systems: Statistical study with DMSP-F7. *Annales de Geophysique*, 22(8), 2775–2783. https://doi.org/10.5194/angeo-22-2775-2004
- Holappa, L., Asikainen, T., & Mursula, K. (2020). Explicit IMF dependence in geomagnetic activity: Modulation of precipitating electrons. Geophysical Research Letters, 47(4), e2019GL086676. https://doi.org/10.1029/2019gl086676
- Hong, Y. (2023). Data for relative contributions of field-aligned currents and particle precipitation to the inter-hemispheric asymmetry at high latitudes during 2015 St. Patrick Day storm [Dataset]. Zenodo. https://zenodo.org/records/10067390
- Hong, Y., Deng, Y., Zhu, Q., Maute, A., Sheng, C., Welling, D., & Lopez, R. (2021). Impacts of different causes on the inter-hemispheric asymmetry of ionosphere-thermosphere system at mid- and high-latitudes: GITM simulations. Space Weather, 19(11), e2021SW002856. https://doi.org/10.1029/2021SW002856
- Hong, Y., Deng, Y., Zhu, Q., Maute, A., Waters, C., Hairston, M., et al. (2023). Inter-hemispheric asymmetries in the high-latitude electrodynamic forcing and the thermosphere during the October 8-9, 2012 geomagnetic storm: An integrated data-model investigation. Frontiers in Astronomy and Space Sciences, 10, 1062265. https://doi.org/10.3389/fspas.2023.1062265
- lijima, T., Fujii, R., Potemra, T. A., & Saflekos, N. A. (1978). Field-aligned currents in the south polar cusp and their relationship to the interplanetary magnetic field. *Journal of Geophysical Research*, 83(A12), 5595–5603. https://doi.org/10.1029/ja083ia12p05595
- Lijima, T., & Potemra, T. A. (1976a). The amplitude distribution of field-aligned currents at northern high latitudes observed by TRIAD. Journal of Geophysical Research, 81(13), 2165–2174. https://doi.org/10.1029/JA081i013p02165
- lijima, T., & Potemra, T. A. (1976b). Field-aligned currents in the dayside cusp observed by TRIAD. *Journal of Geophysical Research*, 81(34), 5971–5979. https://doi.org/10.1029/JA081i034p05971
- Jørgensen, T. S., Friis-Christensen, E., & Wilhjelm, J. (1972). Interplanetary magnetic field direction and high latitude ionospheric currents. Journal of Geophysical Research, 77(10), 1976–1977. https://doi.org/10.1029/JA077i010p01976
- Kamide, Y., & Kusano, K. (2015). No major solar flares but the largest geomagnetic storm in the present solar cycle. *Space Weather*, 13(6), 365–367. https://doi.org/10.1002/2015SW001213
- Knight, S. (1973). Parallel electric fields. Planetary and Space Science, 21(5), 741–750. https://doi.org/10.1016/0032-0633(73)90093-7
- Knipp, D., Kilcommons, L., Hairston, M., & Coley, W. R. (2021). Hemispheric asymmetries in poynting flux derived from DMSP spacecraft. Geophysical Research Letters, 48(17), e2021GL094781. https://doi.org/10.1029/2021GL094781
- Korth, H., Anderson, B. J., & Waters, C. L. (2010). Statistical analysis of the dependence of large-scale Birkeland currents on solar wind parameters. Annales de Geophysique, 28(2), 515–530. https://doi.org/10.5194/angeo-28-515-2010
- Korth, H., Zhang, Y., Anderson, B. J., Sotirelis, T., & Waters, C. L. (2014). Statistical relationship between large-scale upward field-aligned currents and electron precipitation. *Journal of Geophysical Research: Space Physics*, 119(8), 6715–6731. https://doi.org/10.1002/ 2014JA019961
- Larsen, B. A., Morley, S. K., Niehof, J. T., & Welling, D. T. (2021). Spacepy [Dataset]. Zenodo. https://doi.org/10.5281/zenodo.3252523
- Laundal, K. M., Cnossen, I., Milan, S. E., Haaland, S. E., Coxon, J., Pedatella, N. M., et al. (2017). North-South asymmetries in Earth's magnetic field. Space Science Reviews, 206(1–4), 225–257. https://doi.org/10.1007/s11214-016-0273-0

HONG ET AL. 16 of 18



## Journal of Geophysical Research: Space Physics

- 10.1029/2023JA032279
- Laundal, K. M., & Richmond, A. D. (2017). Magnetic coordinate systems. Space Science Reviews, 206(1-4), 27-59. https://doi.org/10.1007/s11214-016-0275-v
- Lin, C. Y., Deng, Y., Sheng, C., & Drob, D. P. (2017). A study of the nonlinear response of the upper atmosphere to episodic and stochastic acoustic-gravity wave forcing. *Journal of Geophysical Research: Space Physics*, 122(1), 1178–1198. https://doi.org/10.1002/2016JA022930
- Liou, K., Newell, P. T., & Meng, C.-I. (2001). Seasonal effects on auroral particle acceleration and precipitation. *Journal of Geophysical Research*, 106(A4), 5531–5542. https://doi.org/10.1029/1999JA000391
- Lu, G. (2017). Large scale high-latitude ionospheric electrodynamic fields and currents. Space Science Reviews, 206(1–4), 431–450. https://doi.org/10.1007/s11214-016-0269-9
- Lu, G., Zakharenkova, I., Cherniak, I., & Dang, T. (2020). Large-scale ionospheric disturbances during the 17 March 2015 storm: A model-data comparative study. Journal of Geophysical Research: Space Physics, 125(5), e2019JA027726. https://doi.org/10.1029/2019JA027726
- Maute, A., & Richmond, A. D. (2017). F-region dynamo simulations at low and mid-latitude. Space Science Reviews, 206(1–4), 471–493. https://doi.org/10.1007/s11214-016-0262-3
- Maute, A., Richmond, A. D., Lu, G., Knipp, D. J., Shi, Y., & Anderson, B. (2021). Magnetosphere-ionosphere coupling via prescribed field-aligned current simulated by the TIEGCM. *Journal of Geophysical Research: Space Physics*, 126(1), e2020JA028665. https://doi.org/10.1029/2020JA028665
- Milan, S. E., Clausen, L. B. N., Coxon, J. C., Carter, J. A., Walach, M.-T., Laundal, K., et al. (2017). Overview of solar wind–magnetosphere–ionosphere–atmosphere coupling and the generation of magnetospheric currents. Space Science Reviews, 206(1–4), 547–573. https://doi.org/10.1007/s11214-017-0333-0
- Milan, S. E., Hutchinson, J., Boakes, P. D., & Hubert, B. (2009). Influences on the radius of the auroral oval. *Annales de Geophysique*, 27(7), 2913–2924. https://doi.org/10.5194/angeo-27-2913-2009
- Newell, P. T., Lyons, K. M., & Meng, C.-I. (1996). A large survey of electron acceleration events. *Journal of Geophysical Research*, 101(A2), 2599–2614. https://doi.org/10.1029/95JA03147
- Nishitani, N., Papitashvili, V. O., Ogawa, T., Sato, N., Yamagishi, H., Yukimatu, A. S., & Rich, F. J. (2003). Interhemispheric asymmetry of the high-latitude ionospheric convection on 11–12 May 1999. *Journal of Geophysical Research*, 108(A5), 1184. https://doi.org/10.1029/ 2002JA009680
- Ohtani, S., Wing, S., Merkin, V. G., & Higuchi, T. (2014). Solar cycle dependence of nightside field-aligned currents: Effects of dayside ionospheric conductivity on the solar wind-magnetosphere-ionosphere coupling. *Journal of Geophysical Research: Space Physics*, 119(1), 322–334. https://doi.org/10.1002/2013JA019410
- Ohtani, S., Wing, S., Ueno, G., & Higuchi, T. (2009). Dependence of premidnight field-aligned currents and particle precipitation on solar illumination. *Journal of Geophysical Research*, 114(A12), A12205. https://doi.org/10.1029/2009JA014115
- Østgaard, N., & Laundal, K. M. (2012). Auroral asymmetries in the conjugate hemispheres and interhemispheric currents. In A. Keiling, E. Donovan, F. Bagenal, & T. Karlsson (Eds.), Auroral phenomenology and magnetospheric processes: Earth and other planets, Geophysical Monograph Series (pp. 99–111). AGU. https://doi.org/10.1029/2011GM001190
- Pakhotin, I. P., Mann, I. R., Xie, K., Burchill, J. K., & Knudsen, D. J. (2021). Northern preference for terrestrial electromagnetic energy input from space weather. *Nature Communications*, 21(1), 199. https://doi.org/10.1038/s41467-020-20450-3
- Park, K. S., Ogino, T., & Walker, R. J. (2006). On the importance of antiparallel reconnection when the dipole tilt and IMF by are nonzero. *Journal of Geophysical Research*, 111(A5), A05202. https://doi.org/10.1029/2004JA010972
- Reiff, P. H., & Burch, J. L. (1985). IMF By-dependent plasma flow and Birkeland currents in the dayside magnetosphere: 2. A global model for northward and southward IMF. *Journal of Geophysical Research*, 90(A2), 1595–1609. https://doi.org/10.1029/JA090iA02p01595
- Reistad, J. P., Laundal, K. M., Ohma, A., Moretto, T., & Milan, S. E. (2020). An explicit IMF By dependence on solar wind-magnetosphere coupling. *Geophysical Research Letters*, 47(1), e2019GL086062. https://doi.org/10.1029/2019gl086062
- Rich, F. J., & Hairston, M. (1994). Large-scale convection patterns observed by DMSP. *Journal of Geophysical Research*, 99(A3), 3827–3844. https://doi.org/10.1029/93JA03296
- Richmond, A. D. (1995). Ionospheric electrodynamics using magnetic apex coordinates. *Journal of Geomagnetism and Geoelectricity*, 47(2), 191–212. https://doi.org/10.5636/jgg.47.191
- Ridley, A., Deng, Y., & Toth, G. (2006). The global Ionosphere-Thermosphere model. *Journal of Atmospheric and Solar-Terrestrial Physics*, 68(8), 839–864. https://doi.org/10.1016/j.jastp.2006.01.008
- Ridley, A. J. (2021). Global ionosphere/thermosphere model (GITM) [Software]. Retrieved from https://github.com/aaroniridley/GITM
- Rishbeth, H., & Müller-Wodarg, I. C. F. (2006). Why is there more ionosphere in January than in July? The annual asymmetry in the F2-layer. Annales de Geophysique, 24(12), 3293–3311. https://doi.org/10.5194/angeo-24-3293-2006
- Robinson, R. M., Kaeppler, S. R., Zanetti, L., Anderson, B., Vines, S. K., Korth, H., & Fitzmaurice, A. (2020). Statistical relations between auroral electrical conductances and field-aligned currents at high latitudes. *Journal of Geophysical Research: Space Physics*, 125(7), e2020JA028008. https://doi.org/10.1029/2020JA028008
- Sheng, C., Deng, Y., Chen, Y.-J., Heelis, R. A., & Huang, Y. (2019). Effects of alignment between particle precipitation and ion convection patterns on Joule heating. *Journal of Geophysical Research: Space Physics*, 124(6), 4905–4915. https://doi.org/10.1029/2018JA026446
- Shi, Y., Knipp, D. J., Matsuo, T., Kilcommons, L., & Anderson, B. (2020). Modes of (FACs) variability and their hemispheric asymmetry revealed by inverse and assimilative analysis of iridium magnetometer data. *Journal of Geophysical Research: Space Physics*, 125(2), e2019JA027265. https://doi.org/10.1029/2019JA027265
- Sivla, W. T., Mtumela, Z., & Ogunjobi, O. (2020). Asymmetric behaviour and geomagnetic dependencies of zonal winds in the middle latitude upper thermosphere. Advances in Space Research, 66(2020), 2141–2150. https://doi.org/10.1016/j.asr.2020.07.020
- Sonnerup, B. U. Ö. (1974). Magnetopause reconnection rate. *Journal of Geophysical Research*, 79(10), 1546–1549. https://doi.org/10.1029/ JA079i010p01546
- Southwood, D. J., & Wolf, R. A. (1978). An assessment of the role of precipitation in magnetospheric convection. *Journal of Geophysical Research*, 83(A11), 5227–5232. https://doi.org/10.1029/JA083jA11p05227
- Sutton, E. K., Forbes, J. M., & Knipp, D. J. (2009). Rapid response of the thermosphere to variations in Joule heating. *Journal of Geophysical Research*, 114, A04319. https://doi.org/10.1029/2008JA013667
- Tanaka, T. (2007). Magnetosphere-ionosphere convection as a compound system. Space Science Reviews, 133(1-4), 1-72. https://doi.org/10.1007/s11214-007-9168-4
- Waters, C. L., Anderson, B. J., Green, D. L., Korth, H., Barnes, R. J., & Vanhamaki, H. (2020). Science data products for AMPERE. In M. W. Dunlop & H. Luhr (Eds.), Ionospheric multi-spacecraft analysis tools, ISSI scientific report series (Vol. 17, pp. 141–165). ISBN 978-3-030-26731-5. https://doi.org/10.1007/978-3-030-26732-2

HONG ET AL. 17 of 18

- Weimer, D. R. (2001). Maps of ionospheric field-aligned currents as a function of the interplanetary magnetic field derived from dynamics explorer 2 data. *Journal of Geophysical Research: Space Physics*, 106(A7), 12889–12902. https://doi.org/10.1029/2000ja000295
- Wing, S., Gkioulidou, M., Johnson, J. R., Newell, P. T., & Wang, C.-P. (2013). Auroral particle precipitation characterized by the substorm cycle. Journal of Geophysical Research: Space Physics, 118(3), 1022–1039. https://doi.org/10.1002/jgra.50160
- Xiong, C., Stolle, C., Alken, P., & Rauberg, J. (2020). Relationship between large-scale ionospheric field-aligned currents and electron/ion precipitations: DMSP observations. Earth Planets and Space, 72(1), 1–22. https://doi.org/10.1186/S40623-020-01286
- Zesta, E., Boudouridis, A., Weygand, J. M., Yizengaw, E., Moldwin, M. B., & Chi, P. (2016). Interhemispheric asymmetries in magnetospheric energy input. In T. Fuller-Rowell, E. Yizengaw, P. H. Doherty, & S. Basu (Eds.), Ionospheric Space weather (Vol. 220, p. 1). https://doi.org/10.1002/9781118929216.ch1
- Zhu, Q., Deng, Y., Maute, A., Sheng, C., & Lin, C. Y. (2017). Impact of the vertical dynamics on the thermosphere at low and middle latitudes: GITM simulations. *Journal of Geophysical Research: Space Physics*, 122(6), 6882–6891. https://doi.org/10.1002/2017JA023939
- Zhu, Q., Deng, Y., Richmond, A., Maute, A., Chen, Y.-J., Hairston, M., et al. (2020). Impacts of binning methods on high-latitude electrodynamic forcing: Static versus boundary-oriented binning methods. *Journal of Geophysical Research: Space Physics*, 125(1), e2019JA027270. https://doi.org/10.1029/2019JA027270
- Zhu, Q., Deng, Y., Richmond, A., McGranaghan, R. M., & Maute, A. (2019). Impacts of multiscale FACs on the ionosphere-thermosphere system: GITM simulation. *Journal of Geophysical Research: Space Physics*, 124(5), 3532–3542. https://doi.org/10.1029/2018JA026082
- Zhu, Q., Lu, G., & Deng, Y. (2022). Low- and mid-latitude ionospheric response to the 2013 St. Patrick's day geomagnetic storm in the American sector: Global ionosphere thermosphere model simulation. Front. Astron. Space Sci, 9, 916739. https://doi.org/10.3389/fspas.2022.916739
- Zhu, Q., Lu, G., Lei, J., Deng, Y., Doornbos, E., van den IJssel, J., & Siemes, C. (2023). Interhemispheric asymmetry of the thermospheric neutral density response to the 7–9 September 2017 geomagnetic storms. *Geophysical Research Letters*, 50(11), e2023GL103208. https://doi.org/10.1029/2023GL103208
- Zhu, Q., Lu, G., Maute, A., Deng, Y., & Anderson, B. (2022). Assessment of using field-aligned currents to drive the global ionosphere thermosphere model: A case study for the 2013 St Patrick's day geomagnetic storm. *Space Weather*, 20(9), e2022SW003170. https://doi.org/10.1029/2022SW003170

HONG ET AL. 18 of 18